Design and Analysis of a MEMS Fabry-Perot Pressure Sensor

by

Sohrab Haghighat

A thesis
presented to the University of Waterloo
in fulfillment of the
thesis requirement for the degree of
Master of Applied Science
in
Mechanical Engineering

Waterloo, Ontario, Canada, 2007

AUTHOR'S DECLARATION

I hereby declare that I am the sole author of this thesis. This is a true copy of the thesis, including any required final revisions, as accepted by my examiners.

I understand that my thesis may be made electronically available to the public.

Abstract

Accurate dynamic pressure measurements in the jet engine compressors are the key point in the detection of instabilities that are often precursors to surge or rotating stall. Localized pressure measurements are also very helpful in vehicles aerodynamics performance optimization. A new MEMS pressure sensor capable of measuring pressures between 14.7 psi to 100 psi is presented in this work. The sensor is based on the effect of the viscous damping force on the frequency response of a micro cantilever beam. The frequency response of a micro cantilever beam is affected by two types of damping, squeeze film damping and air flow damping. Both these effects are modeled here. The airflow damping is dependent on the air pressure and increases with pressure. This sensitivity to pressure is utilized to predict the ambient air pressure. In order to measure the beam frequency response, a Fabry-Perot interferometer is fabricated using the cantilever beam and the substrate. An electro-optical measurement system is setup to measure the frequency response of the sensor.

A custom made pressure chamber is designed and fabricated to allow high pressure tests. The measured frequency response of the cantilever beams are compared with the model results. The experimental results are fitted to the model predictions using pressure as the fitting parameter. The estimated pressure is then compared with the applied pressure. The estimated pressure is in good agreement with the actual pressure for pressures below *40 psi*. For the PolyMUMPs fabricated sensors, the error is less than 4% for pressure values smaller than *40 psi.*

Acknowledgements

I would like to thank my supervisors, Prof. Patricia Nieva and Prof. Amir Khajehpour, whose guidance, patience and encouragement helped me during my research. I also thank them for their valuable suggestions during writing of this thesis.

I would like to express my thanks to the staff of Department of Mechanical and Mechatronics Engineering of the University of Waterloo. A special thanks is offered to Robert Wagner and John Potzold for their assistance in fabricating the pressure chamber.

I am very grateful to Wood Chiang for his assistance in the electronics set up. I would like to thank my friends and co-workers for their support: Kamran Shavezipour, Syed and Jim Kuo. My special thanks goes to my friend Ashkan Rasouli for his support in the thesis preparation.

I would like to express my sincere thanks to my girlfriend, Saharnaz Safari. It was her support, understanding and encouragement over the course of my thesis preparation which made this work possible.

Finally, I would like to thank my parents, Nahid and Behrouz Haghighat and my sisters, Sogol and Nazgol for their patience, care and emotional support.

Table of Contents

List of Figures

Insert List of Figures here.

List of Tables

Chapter 1
Introduction

Increasing the measurement accuracy and expanding the operating conditions of sensors pushes the limits of the available sensing technology. Sensors using the current technology can be used in most environmental conditions and provide a broad measurement range. However, there are at least two operating regimes where the current technology fails to meet the minimum requirements; environments with either high temperatures and/or high electromagnetic interference. These harsh environments require special sensing devices adapted to suit the environment.

There is an increasing consumer demand for harsh environment sensing devices. One of the most demanding consumers of these sensors is aerospace industries. In aerospace industries, and especially in propulsion systems, the need to obtain transient localized measurements motivates sensor designers to use micro machined sensors. Some applications include flow control systems for improving aerodynamic performance of flying vehicles or active surge control for jet engines.

The need to monitor flow conditions in harsh environments for performance evaluation and control of new propulsion systems is one of the most challenging applications of micro sensors. Control methodologies developed to avoid high-cycle fatigue (HCF), combustion instabilities or compressor surge will require sensors capable of operating in the engine environment. The flow environment inside an operating propulsion system is under high temperature (Figure 1.1) and a considerable demand is placed on sensor and instrumentation technology.

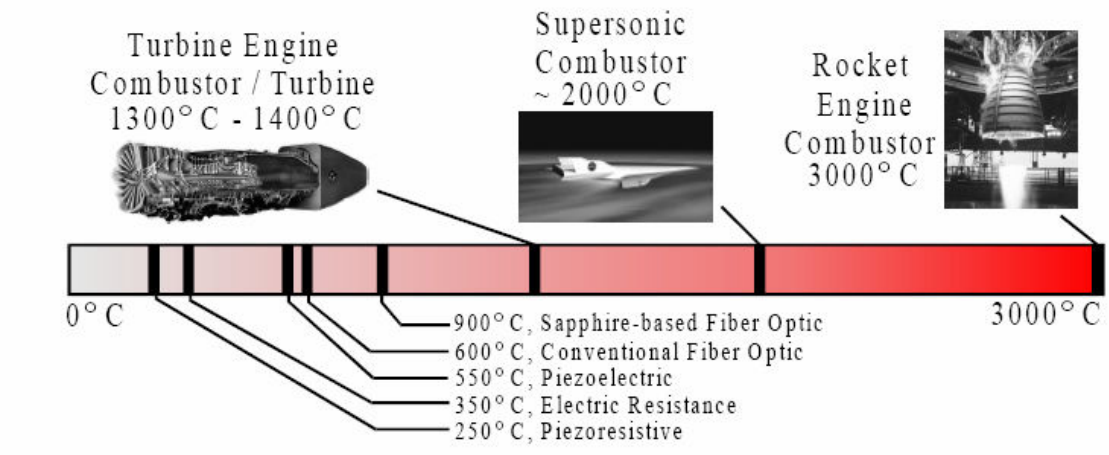

Figure 1.1 High temperature regimes for sensors for aerospace application [1]

Currently, engine designers have to consider a significant safety margin for the compressor to protect the engine from surging. The total amount of this margin is typically on the order of 35%, meaning the engine is carrying 35% more compressor stages than it needs for steady-state operation. This safety margin results in extra cost, weight, compressor length and part count. Using active compressor surge control, it is possible to eliminate a stage of compression from the engine which can have the following benefits for a typical military engine [1]:

- +5% thrust/weight
- -1.5% thrust specific fuel consumption
- -3.2% acquisition cost
- -1% operating cost

- Surge free operations
- Extension of maintenance intervals
- Increase inlet distortion envelope

Accurate dynamic pressure and temperature measurements in the compressor are the key point in the detection of instabilities that are often precursors to surge or rotating stall. Hence, developing sensors that can operate in the compressor environment is a significant step forward to realization of the active surge control system.

In addition to the application of harsh environment sensors to engine performance optimization, they can be used to provide accurate data for aerodynamics designs. Measurement of shear stress and temperature in complex flows is of great importance and interest, since detailed knowledge of shear stress and boundary layer separation has a first-order role in the design process of aerodynamic vehicles. Specially, measuring shear stress and temperature in high temperature turbulent boundary layer could be used to improve turbulence and heat transfer models that are critical for advanced designs [2].

Vibration sensors for harsh environment also have a critical role in optimizing the mechanical design of machinery. Due to their small size and low weight, micro sensors do not affect the response of the moving body and will be an ideal option for vibration measurements. Reliability analysis of mechanical systems is one of the important applications of the micro vibration sensors, especially the reliability study of modern and sophisticated pieces of machinery. One example is the gas turbine engine which its health condition is related in part to the frequency, amplitude and location of vibrations in its

system. Having components that operate at temperatures as high as 600 ^{o}C, the turbine engine system can benefit from using vibration sensors that tolerate high temperatures [3].

The combination of high temperature tolerance and high frequency response cannot be met by currently available sensors.

This work presents a new conceptual design for a pressure sensor that can be operated at high temperatures. The pressure sensor developed in this work is based on the fact that the response of a resonator depends on the damping factor of the system especially, for frequencies close to the natural frequency. A suspended cantilever beam is used as the resonator here. A cantilever beam is used to avoid the effect of the axial forces on the system response. It has be shown that plates and clamped-clamped beams frequency response changes with the axial force. The axial force in plates and doubly clamped beams can be generated due to the temperature expansion coefficients. To be able to characterize the proposed pressure sensor, different energy dissipation sources and the effect of pressure on them have to be considered. There are several mechanisms of energy dissipation that affect the performance of a micro resonator. The most common energy dissipation mechanisms are the losses due to air viscosity, the support losses and the intrinsic damping caused by losses inside the material. Among all of those energy dissipation sources, viscous damping forces are dominant and the other damping sources can be neglected [2, 3, 11].

The viscous damping force can be divided into two categories. One is the force in the free space and the other one is the force in the narrow gap [1,2].

The squeeze damping force arises from the pressure difference between the ambient air and the air trapped in the narrow gap between the structure and its substrate. This mechanism has been studied extensively [1,2,4-9] and its analysis is usually done by solving the Reynolds' equation for an isothermal incompressible gas between two solid flat plates. In this case, the microstructure is assumed to be rigid in order to decouple the fluid-structure interaction problem and obtain a closed form solution [1,2,3-8]. However, a vibrating microbeam is a deformable body; hence the air gap height varies across the length of the beam. In this work, the elastic beam theory is coupled to the linearized Reynolds' equation for small amplitudes of oscillation to calculate the frequency response of a microcantilever beam undergoing excitation on the base. The pressure distribution underneath the beam is approximated by a power series and the squeeze film damping is calculated by integrating the pressure distribution. The airflow damping is also modeled and considered using the beads model presented by *Hosaka et al* [21-23]. This is the damping term that varies with pressure.

The free standing cantilever beam and the substrate develop a Fabry-Perot interferometer with the substrate. The Interferometer is used for the readout to detect the beam movement. advantages of the optical sensors over the conventional electrical sensors include the immunity to electromagnetic interference, resistance to harsh environment and capability for multiplexing. Fabry-Perot interferometer used in this work consists of two partially reflecting parallel mirrors separated by an air gap. With this structure, one can easily measure a loaded pressure by detecting the changes of the reflected optical signals due to the change of the gap.

Chapter two is devoted to the background review. Different MEMS pressure sensors are presented and their advantages and disadvantages are compared against each other. The working principle of the proposed sensor is also presented in this Chapter.

In Chapter three, the equations of motion of a cantilever beam under the effect of viscous damping are developed. The dependency of the damping factor on the ambient pressure is also shown in Chapter two. Chapter four deals with the optical readout system and relates the beam motion to the optical signal detected by a photodiode. Chapter five describe the test setup used in this work. Fabrication processes are also described in Chapter. To be able to perform high pressure tests, a custom made pressure chamber is design and fabricated. Finally, experimental results are compared with the analytical results in Chapter six. The experimental results are fitted to the model results using pressure as the fitting parameters. The fitted pressures are compared with the applied pressures. The pressure resolution calculations are also presented in Chapter six.

Chapter 2
Background Review

In the first part of this chapter different MEMS pressure, temperature and vibration sensors are presented and their advantages and disadvantages are compared against each other. Following that the working principles of the proposed MEMS pressure sensors is presented.

2.1 Pressure Sensors

Over the past decade, different techniques have been used to measure the pressure of a fluid. In this section different methods that are used in micro sensors are presented and compared to each other.

2.1.1 Piezoresistive Pressure Sensors

In 1954, the piezoresistive effect of silicon and germanium, which is a change of resistance with applied stress, was reported. This discovery enabled production of semiconductor-based sensors. Piezoresistive pressure sensors consist of diaphragms that deform due to the applied pressure. A piezoresistor is mounted on or in the diaphragm to sense the pressure. For thin diaphragms and small deflections, the resistance change is linear with applied pressure [4].

The evolution of piezoresistive pressure sensor technology is illustrated in Figure 2.1 starting with metal diaphragm sensors with bonded silicon strain gauges (Figure 2.1.a). First designs had low yield and poor stability due to such factors as thermal mismatch with the metal–epoxy–silicon interface. Metal diaphragms were quickly superseded by single crystal diaphragms with diffused piezoresistors (Figure 2.1.b). These new types of sensor had many

advantages related to the properties of silicon and the availability of high-quality silicon substrates.

Some of the first silicon diaphragms were created by mechanical milling spark machining followed by wet chemical isotropic etching to create a cup shape (Figure 2.1.b). These diaphragms were bonded to silicon supports, by a gold–silicon eutectic bond (Teutectic = 370 oC). While this technique of fabrication had the advantages of increased sensitivity and reduced size, the cost was still high, and diaphragms were created one at a time, rather than in a batch mode [4].

By the late 1960s and early 1970s, three key technologies were being developed: anisotropic chemical etching of silicon, ion implantation, and anodic bonding [4]. Ion implantation was used to place strain gauges in single-crystal silicon diaphragms. Ion implantation is generally better than diffusion for doping because both the doping concentration and doping uniformity are more tightly controlled. Anisotropic etching improved the diaphragm fabrication process in a number of ways:

- diaphragm sizes and locations were now well controlled by IC photolithography techniques
- strain gauge placements were improved
- anisotropic etching was well suited to batch fabrication, allowing hundreds of diaphragms to be created simultaneously
- overall size was decreased further

Anisotropic etching and anodic bonding are batch techniques, and hence hundreds of pressure sensors can be manufactured simultaneously on a single wafer. This is a significant cost reduction when compared to previous technologies. A representative sensor from this period is shown in Figure 2.1.c. By using micromachining technology the dimensions of the diaphragm are shrinking to hundreds of micrometers and the minimum feature sizes are reduced to micrometers (Figure 2.1.d).

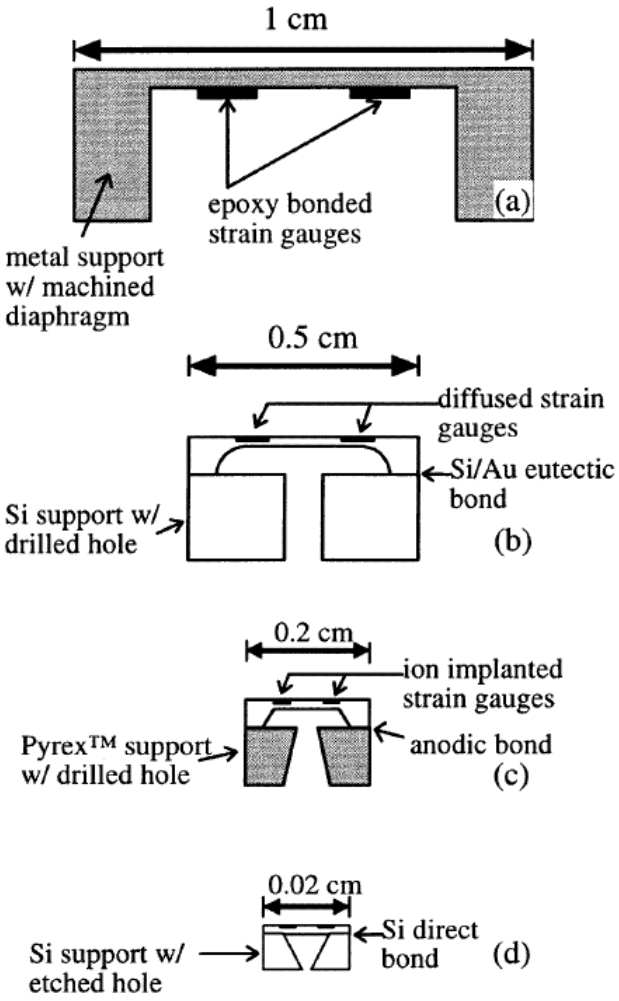

Figure 2.1 The evolution of diaphragm pressure sensor (adapted from [4])

Anisotropic etching and bonding technologies have also been improved. The direct bonding method was first reported in 1985. This method was first used for making silicon-on-insulator (SOI) material, but was quickly applied to micromachined devices. Also, surface-micromachined devices have been reported, which have silicon nitride or polysilicon diaphragms. These sensors have decreased die size and may simplify integration with electronics, but at the cost of reduced sensitivity and reproducibility of mechanical properties.

2.1.2 Capacitive Pressure Sensors

Capacitive sensors are based upon parallel plate capacitors. A typical bulk micromachined capacitive pressure sensor and pressure-capacitance response of one such sensor is shown in Figure 2.2.

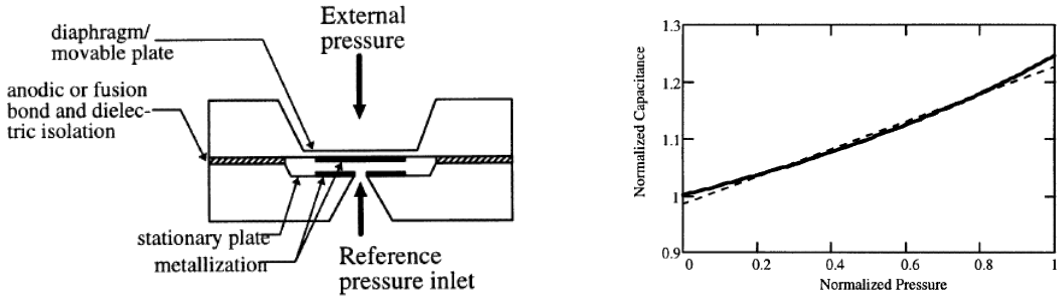

Figure 2.2 A cross section schematic diagram of capacitive pressure sensor [4]

The principal advantages of capacitive pressure sensors over piezoresistive pressure sensors are increased pressure sensitivity and decreased temperature sensitivity. However, there are some serious disadvantages which affect the popularity of capacitive sensors. In contrast to piezoresistive sensor which has a linear response, capacitive sensors usually have the disadvantage of exhibiting nonlinear behaviour [5]. To fix this problem, a capacitive

sensor can be operated in contact mode to increase linearity (Figure 2.3). In contact mode, the capacitance is nearly proportional to the contact area, which in turn shows good linearity with respect to applied pressure. This holds true over a wide range of pressures. However, this linearity comes at the expense of sensitivity.

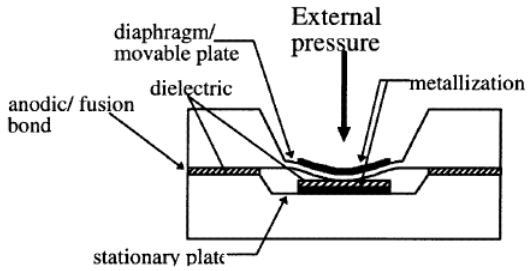

Figure 2.3 A cross section schematic diagram of a contact mode pressure sensor [4]

Another method for achieving a linear response is to use bossed diaphragms. Figure 2.4 illustrates this concept. The left drawing is a cut-away view of a uniform-thickness diaphragm and its corresponding cross-sectional deflected mode shape. A non-uniform, bossed diaphragm is on the right. The thicker centre portion (or boss) is much stiffer than the thinner arms on the outside. The centre boss contributes most of the capacitance of the structure and its shape does not distort appreciably under applied load. Hence the capacitance–pressure characteristics will be more linear.

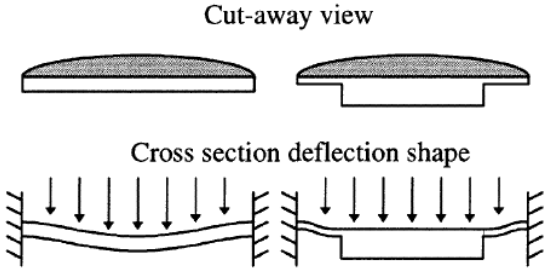

Figure 2.4 A comparison of deflected shapes for uniform-thickness and bossed diaphragm [4]

Excessive signal loss from parasitic capacitance is one serious disadvantage, which hindered the development of miniaturized capacitive sensors until on-chip circuitry could be fabricated.

2.1.3 Optical Pressure Sensor

Many diaphragm-based optical sensors have been reported which measure pressure induced deflections by Mach–Zehnder and Fabry–Perot interferometry methods. Figure 2.5 shows a typical Fabry-Perot optical pressure sensor.

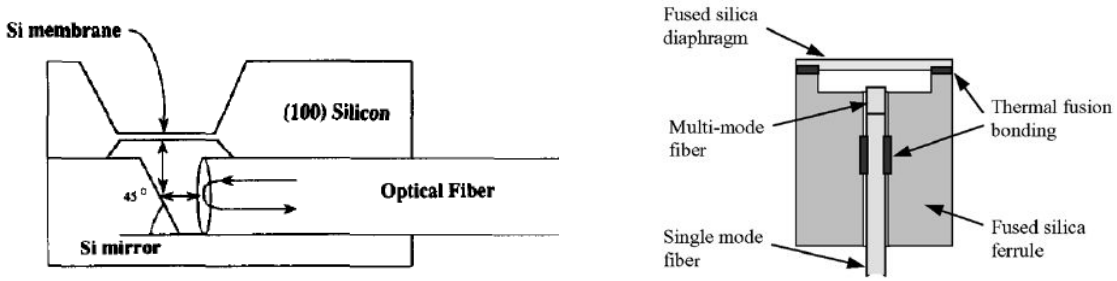

Figure 2.5 Schematic diagrams of Fabry-Perot optical pressure sensors [6,7]

A Fabry-Perot interferometer consists of an optical cavity situated between two reflecting mirrors. Typically, the two mirrors are parallel, with one mirror totally reflecting and capable of spatial translation while the other mirror is partially transparent and stationary. Interference between multiple reflections causes the power reflectance of the received signal to be a function of cavity's optical path length [7].

The deflection derived from these devices varies linearly with pressure. Optical pressure sensors have a number of potential advantages in comparison with their electrical

counterparts. They are less sensitive to electromagnetic interference, can be used in high temperature environments, and do not require wire bonding [6].

Although these sensors can be used in harsh environments, they often suffer from temperature sensitivity problem. This problem can be solved by considering the effect of thermal expansion using the coefficient of thermal expansion of employed materials [6].

2.1.4 Resonant Pressure Sensors

One of the new classes of pressure sensors reported in recent years is the resonant beam pressure sensor. These sensors operate by monitoring the resonant frequency of an embedded doubly clamped bridge or comb drive. The resonant beam, which has also been called a resonating beam force transducer, acts as a sensitive strain gauge. As the stress state of the diaphragm changes, the tension in the embedded structures changes and so does the resonant frequency. There have been several mechanisms reported by which the structures can be driven into resonance while the resonant frequency is being sensed. One method is electrostatic excitation and piezoresistive sensing. The structure is driven by AC applied voltages, and the resonant frequency is measured by piezoresistors. Structures can also be excited using electrostatic forces and the resonant frequency can be sensed using the capacitance of the sensor [8]. Resonant pressure sensors have been shown to exhibit better pressure sensitivity and lower temperature sensitivity than pure piezoresistive sensors. Furthermore, a frequency output is more immune to noise than classical analogue piezoresistive and capacitive signals.

2.2 Temperature Sensors

Thermal sensors are used to measure various heat-related quantities such as temperature, heat flux and heat capacity. Among these quantities, temperature is perhaps the most fundamental variable. Thermal sensors form the largest and perhaps the most important class of microsensors today. About 40% of all solid-state sensors commercially sold are thermal sensors [9]. Thermal sensors can be classified either as contacting or non-contacting [9, 10].

Contacting sensors physically touch the heat source or sink of interest. The thermal signal then propagates from the source (or the sink) to the sensing element, which in response either generates or modulates an electrical signal. On the other hand, non-contacting thermal sensors sense heat remotely, without physically touching the source (or the sink). While a few thermal-electrical sensors are self-generating, such as a thermocouple generating a temperature-dependent electromotive force, the majority are modulating. Many of the thermo-conductive sensors, such as thermoresistors, thermodiodes, or thermotransistors, can be made as microsensors and used to measure a wide range of temperatures from as low as 1.5 K to as high as 2700 K [9].

2.2.1 Thermistor Temperature Sensors

The working principle of thermistors is based on the temperature dependence of the electrical resistivity of the materials. Although the resistivity of both metals and semiconductors vary with temperature, their behaviour can be quite different. In metals, the resistivity change is essentially caused by changes in carrier mobility, which typically increases with temperature because of enhanced photon scattering. On the other hand, greater sensitivity can be obtained in highly resistant single crystalline semiconducting materials, in which the free carrier

concentration increases exponentially with temperature. Thermistors are usually built on polycrystalline semiconducting thin films [9].

2.2.2 Piezoelectric Temperature Sensors

The piezoelectric effect is a temperature dependent phenomenon. Thus, a temperature sensor based on variability of oscillating frequency of vibrating member can be designed. The temperature dependence of the resonant frequency can be approximately expressed by a third order polynomial. However, a very successful development of a linear temperature sensor has been reported by Hewlett-Packard [10]. The sensitivity of sensor is 35 ppm oC-1 and it has an operating range of -80 to 230 oC. With the advent of microprocessors, linearity became a less important factor and more sensitive sensors (90 ppm oC-1) were fabricated [10].

2.2.3 Optical Temperature Sensors:

There are situations that temperature has to be measured at harsh environments where electrical bonding can not be used. One way to solve this problem is to use non-contact methods of temperature measurements, such as optical sensing.

Similar to optical pressure sensors, Fabry-Perot interferometry can be used as a temperature detection technique. The working principle is the same as optical pressure sensors. The key point for temperature detection in this method is using a material that its refractive index is a function of temperature [10].

2.3 Vibration Sensors

A vibration sensor can be thought of as a very highly sensitive accelerometer with no direct current (dc) output requirement. Applications for these devices include geophysical sensing, machinery vibration and failure prediction, tracking and identification of vehicles or personnel, and underwater pressure gradient sensing [11]. Most vibration sensors (displacement sensors or accelerometers) are based on a suspended proof mass which is connected to the case using springs (Figure 2.6). Vibration sensors use the displacement of the base as the excitation mechanism for the proof mass. The relative displacement of the proof mass with respect to the case is a function of the base vibration amplitude and frequency.

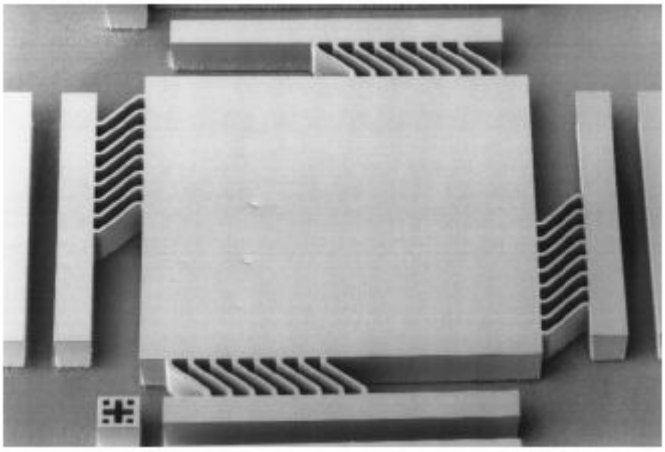

Figure 2.6 Vibration sensor structure etched through a 380 μm wafer [11]

When the ratio of working frequency over the sensor's natural frequency becomes very small, the relative displacement of the suspended mass becomes proportional to the acceleration. In this case the sensor can be used as an accelerometer. However, if the sensor's natural frequency is small compared to the working frequency, the relative displacement

approaches the displacement of the case. This type of sensor can be used as a displacement sensor [12].

Although the most vibration sensors use the same working principle, different transduction techniques can be used for detecting minute displacement of the proof mass. These techniques include the measurement of charge across a variable capacitor, change in resistance of a piezoresistive material and measuring the power reflectance of a reflected signal [11, 13]. Figure 2.7 shows a schematic diagram of a fully-integrated version of an optical displacement sensor. Among these techniques, the Fabry-Perot method shows better sensitivity to displacement and is less susceptible to electromagnetic noises.

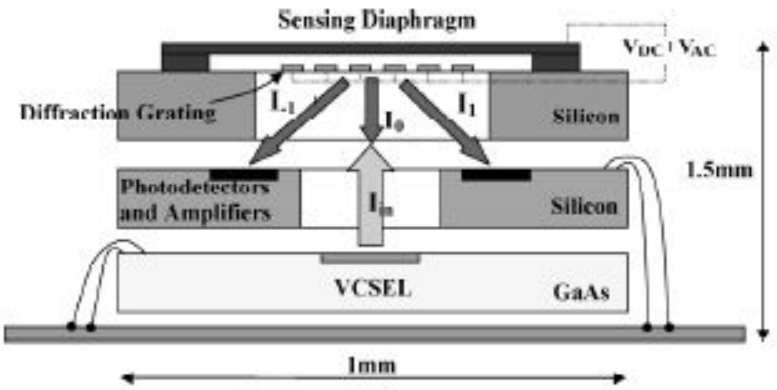

Figure 2.7 Schematic diagram of a fully-integrated version of an optical displacement sensor [14]

2.4 Proposed pressure sensor working principle

In previous sections different types of fabricated pressure, temperature and displacement sensors were presented. As it is stated, almost all pressure sensors are based on the deflection of a diaphragm. On the other hand, displacement sensors are based on the movement of a suspended mass. This proof mass is usually operated in vacuum condition and the air parameters do not affect its movement. However, if a system of mass/spring is operated in a fluid medium the pressure and temperature of the fluid can affect the displacement of the proof mass. The displacement sensitivity to the air pressure can be used as an idea for developing a new pressure sensor.

A simple lumped mass analysis shows that the frequency response of a vibrating proof mass at frequencies close to the natural frequency of the system is highly dependent on the damping factor. The damping factor for a suspended micro cantilever beam depends on the fluid characteristics and can be categorized into squeezed film and airflow damping. Squeezed film damping is due to the movement of fluid particles between two parallel plates moving normal to each other and is a function of viscosity which itself can be stated as a function of temperature. On the other hand, the airflow damping is the resistance applied by fluid particles on a moving body in free space and can be related to viscosity which depends on temperature and density which depends on both temperature and pressure. By exciting a cantilever beam with a known displacement at a predefined frequency (close to the natural frequency), the ambient pressure can be calculated. This idea is used as the working principle of the proposed sensor.

As presented in this chapter, different techniques have been used to detect the movement/deformation of the diaphragms. Among all techniques, Fabry-Perot interferometry is reported to be the best type of transduction for harsh environment, since they are less sensitive to electromagnetic interference, can be used in high temperature environments, and do not require wire bonding [6]. This technique is used in this work to measure the cantilever beam displacement.

Chapter 3
Mechanical Analysis

This chapter presents the vibrational analysis of a cantilever beam that undergoes a harmonic excitation. The schematic drawing of the cantilever beam is shown in Figure 3.1. Since the length of the beam is much longer than its width and also the thickness of the beam is very small compared to the other dimensions, the Euler-Bernouli beam theory can be used to model the cantilever beam deflection.

The substrate undergoes a harmonic excitation ($Z_0 e^{i\omega t}$) and the cantilever beam responds to the base motion , $z(x,t)$, which is a function of position *x* and time *t*. Consider the cantilever beam shown in Figure 3.1, with length, width and thickness *l*, *b* and *d*, respectively. The thickness of the air gap between the beam and the substrate at the anchor is h_0. The Equation of motion of the beam is:

$$\frac{\partial^2}{\partial x^2}\left[EI \frac{\partial^2 z(x,t)}{\partial x^2} \right] + \rho bd \frac{\partial^2 z(x,t)}{\partial t^2} = f(x,t) \tag{3.1}$$

where *E, I* and ρ are the Young's modulus, the moment of inertia ($I = wd^3/12$) and the density of beam. *f(x,t)* is the external force per unit length of the beam. Assuming the beam cross section does not change along the *x* direction, the equation will be as follows:

$$EI\frac{\partial^4 z(x,t)}{\partial x^4}+\rho bd\frac{\partial^2 z(x,t)}{\partial t^2}=f(x,t) \tag{3.2}$$

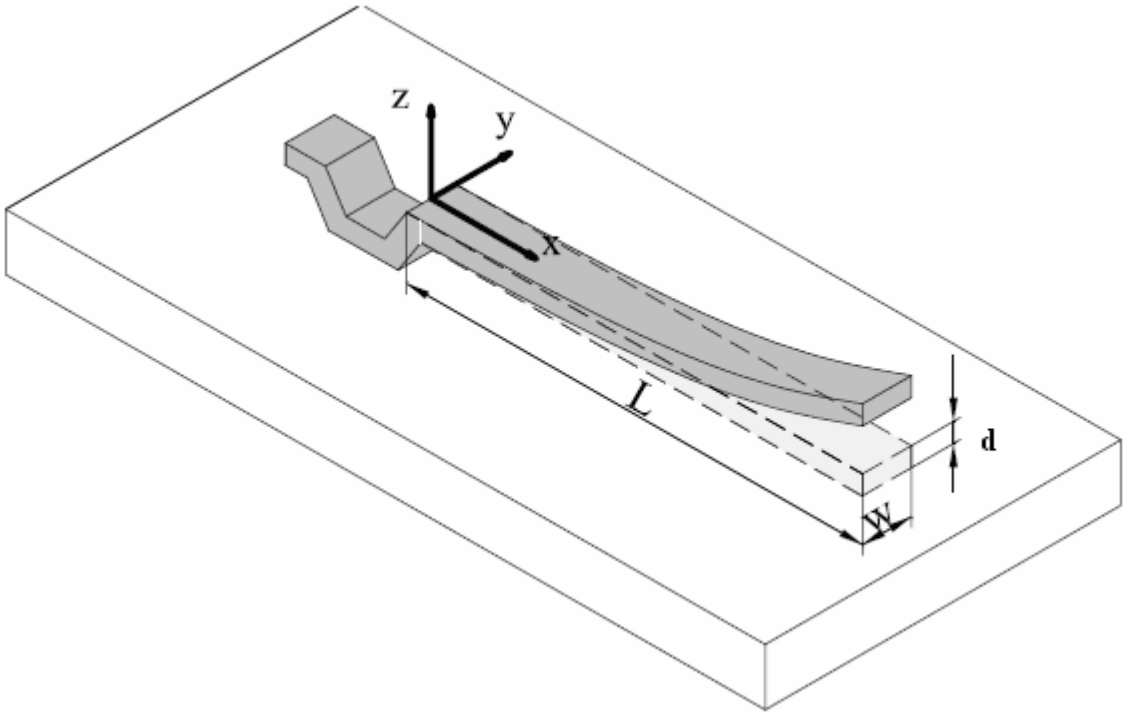

Figure 3.1 Schematic Configuration of a Micro Cantilever Beam. This figure is too far away from the equation of motion

In most MEMS devices like capacitors or filters the relative displacement is the governing parameter. In addition measurement techniques which have bean used in MEMS, such as capacitance measurement or optical interferometery, are capable of measuring the relative motion between two parallel plates. Hence, the *Euler-Bernoulli* equation can be rewritten using the relative displacement (δ_r) of:

$$\delta_r(x,t)=z(x,t)-Z_0e^{i\omega t} \tag{3.3}$$

Substituting the above equation into Equation (3.2), the *Euler-Bernoulli* equation can be re-arranged as:

$$EI\frac{\partial^4\delta_r}{\partial x^4}+\rho bd\frac{\partial^2\delta_r}{\partial t^2}=f(x,t)+\underbrace{Z_0\rho bd\omega^2 e^{i\omega t}}_{f_H} \tag{3.4}$$

The term f_H is the harmonic force per unit length due to the base vibration. As we can see from Figure 3.1 the cantilever beam is fixed at the anchor ($x=0$) which can be expressed using:

$$\delta_r(0,t)=\frac{\partial}{\partial x}\delta_r(0,t)=0 \tag{3.5}$$

while the cantilever beam is free at the other end ($x=l$) and no force and no moment are applied. The other two boundary conditions are:

$$\frac{\partial^2}{\partial x^2}\delta_r(0,t)=\frac{\partial^3}{\partial x^3}\delta_r(0,t)=0 \tag{3.6}$$

For the cantilever beam shown in Figure 3.1 which undergoes an out of plane motion, two sources of the external forces exist. One is the squeeze film damping and the other one is the air flow damping. When the beam is moving up and down the air is sucked into or compressed out of the narrow gap below the beam, respectively. This process causes a pressure difference in the narrow gap which itself creates a force called *squeeze film* damping force [3].

When a beam or a plate is moving in a free space, it also experiences a force applied by the surrounding fluid to the beam. This force is applied to any structure moving in a fluid

(aerodynamic drag force) and is called the *airflow* damping force. These two damping forces have a great influence on the cantilever motion and the frequency response of the beam and will be the focus of this chapter.

3.1 Squeeze Film Damping

To find the pressure distribution in the narrow gap we start with the Navier-Stokes equations. The selected control volume is shown in Figure 3.2. The Reynolds' number for a micro scale cantilever beam is very small ($Re<<1$) [3,21]. Hence, the inertia and gravitational terms in the Navier-Stokes equations can be neglected [15]. The simplified Navier-Stokes equations are:

$$\frac{\partial p}{\partial x} = \frac{\partial}{\partial z}(\mu \frac{\partial u}{\partial z}) \tag{3.7}$$

$$\frac{\partial p}{\partial y} = \frac{\partial}{\partial z}(\mu \frac{\partial v}{\partial z}) \tag{3.8}$$

$$\frac{\partial p}{\partial z} = 0 \tag{3.9}$$

Where u, v are air particle velocities in x and y directions respectively. p is the air pressure and μ is the air viscosity. Equation (3.9) shows that the pressure distribution in the narrow gap does not vary along the gap height (z direction). Assuming the no-slip boundary condition, the boundary conditions will have the following form:

$$\begin{aligned} &at\ z = 0;\ \ u(x,y,z) = 0,\ v(x,y,z) = 0 \\ &at\ z = -h_0;\ \ u(x,y,z) = 0,\ v(x,y,z) = 0 \end{aligned} \tag{3.10}$$

Considering the above boundary conditions and solving the differential Equations (3.7) and (3.8), the fluid particle velocities can be found as follows:

$$u(x,y,z) = \frac{1}{2\mu}\left(\frac{\partial p}{\partial x}\right)(z^2 - zh)$$
$$v(x,y,z) = \frac{1}{2\mu}\left(\frac{\partial p}{\partial v}\right)(z^2 - zh) \tag{3.11}$$

where h is the gap height at each point which is a function of x and y.

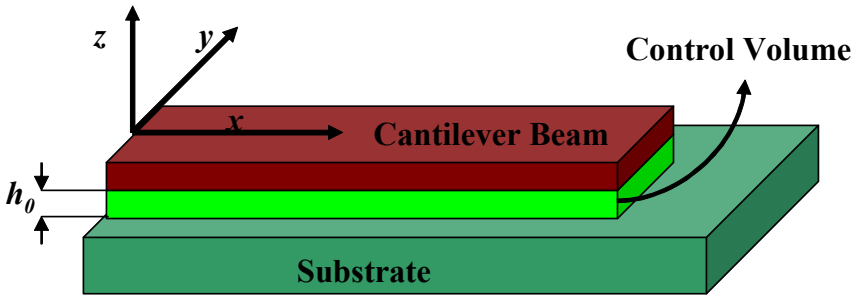

Figure 3.2 Control volume for the squeeze film damping analysis

Calculating the flow rate per unit width in x and y direction and substituting in the continuity equation, the Reynolds' equation can be found as follows:

$$-\frac{\partial}{\partial x}\left(ph^3\frac{\partial p}{\partial x}\right) - \frac{\partial}{\partial y}\left(ph^3\frac{\partial p}{\partial y}\right) = 12\mu\frac{\partial}{\partial t}(ph) \tag{3.12}$$

The Reynolds' equation is derived under the isothermal assumption. It expresses the pressure distribution in the narrow gap below the beam in x and y direction. The boundary conditions for this partial differential equation for the geometry under investigation are as follows:

$$p\left(x, \pm\frac{b}{2}, t\right) = p(l, y, t) = p_a \tag{3.13}$$

$$\frac{\partial}{\partial x} p(0, y, t) = 0 \tag{3.14}$$

The first term indicates that the pressure at the free edges is equal to the ambient pressure (trivial boundary condition) and the second term states that there is no flow into or out of the control volume at the fixed boundary condition (no flux boundary condition). To find the squeeze film damping force, the pressure distribution below the beam should be solved. Knowing the pressure distribution the squeeze film damping force per unit length can be found as follows:

$$f_{squeeze\ film} = \int_{-\frac{b}{2}}^{\frac{b}{2}} \left(\delta_p\right) dy \tag{3.15}$$

where $\delta_p = p - p_a$

The Reynolds' equation is a nonlinear partial differential equation which makes it difficult to solve analytically. Hence, we start by changing it into a non-dimension nonlinear form. The following non-dimension parameters are introduced:

$$\delta_R = \frac{\delta_r}{h_0},\ \mathrm{H} = \frac{h}{h_0},\ \mathrm{X} = \frac{x}{l},\ \mathrm{Y} = \frac{y}{l},\ \mathrm{T} = \omega t,\ \mathrm{P} = \frac{p}{p_a},\ \delta_P = \frac{\delta_p}{p_a} = P - 1 \tag{3.16}$$

For a deflected beam, the gap height at each point is $h(x) = h_0 + \delta_r(x)$. Assuming the beam undergoes small oscillations ($\delta_R << 1$), the pressure difference can be considered to be very small as well. Using the non-dimension parameters introduced in equation(3.16), the Reynolds' equation can be rewritten as follows:

$$\frac{\partial}{\partial X}\left(H^3 P\frac{\partial P}{\partial X}\right)+\frac{\partial}{\partial Y}\left(H^3 P\frac{\partial P}{\partial Y}\right)=\sigma\frac{\partial(PH)}{\partial T} \tag{3.17}$$

where $\sigma = \frac{12\mu\omega l^2}{P_a h_0^{\,2}}$ is known as the squeeze number.

The boundary conditions for the dimensionless Reynolds' equation will have the following form:

$$\begin{aligned} &P\left(X,\pm\frac{1}{2\beta},T\right)=P(1,Y,T)=1 \\ &\frac{\partial}{\partial X}P(0,Y,T)=0 \end{aligned} \tag{3.18}$$

Substituting P, H with $1+\delta_P$, $1+\delta_R$ respectively, Equations (3.17) and (1.18) can be changed into a linear form:

$$\frac{\partial^2\delta_P}{\partial X^2}+\frac{\partial^2\delta_P}{\partial X^2}-\sigma\frac{\partial\delta_P}{\partial T}=\sigma\frac{\partial\delta_R}{\partial T} \tag{3.19}$$

$$\delta_P(X,\pm\frac{1}{2\beta},T)=\delta_P(1,Y,T)=0 \tag{3.20}$$

$$\frac{\partial}{\partial X}\delta_P(0,Y,T)=0 \tag{3.21}$$

Since, the simplified Reynolds' equation and the Euler-Bernoulli equation in (3.19) and (3.4) are linear, the steady-state response of the system to a harmonic excitation will be a harmonic function with the same frequency. Hence, the steady-state responses will have the following form:

$$\delta_R=\overline{\delta_R}e^{iT},\ \delta_P=\overline{\delta_P}e^{iT} \tag{3.22}$$

Substituting the above equations into Equation(3.19) , we have:

$$\frac{\partial^2\left(\overline{\delta_P}\right)}{\partial X^2}+\frac{\partial^2\left(\overline{\delta_P}\right)}{\partial Y^2}-i\sigma\overline{\delta_P}=i\sigma\overline{\delta_R} \tag{3.23}$$

The left hand side of Equation (3.23) is only a function of pressure while on the right hand side there is the relative displacement. The response of a linear system can be expressed in terms of the mode shapes of the system. The same approach is used here to solve Equation (3.23). The relative displacement on the right hand side of Equation (3.23) can be approximated using the mode shapes of the Euler-Bernoulli Equation (for free vibration $EI\frac{\partial^4\delta_r}{\partial x^4}+\rho bd\frac{\partial^2\delta_r}{\partial t^2}=0$).

$$\overline{\delta_R}=\sum_{i=1}^{\infty}A_i\Phi_i \tag{3.24}$$

where Φ_i are the mode shapes of the Euler-Bernoulli equation and A_i are the mode shapes amplitude.

The mode shapes of a cantilever beam can be found using the following equation:

$$\Phi_i(X)=\cosh\alpha_i X-\cos\alpha_i X-\left[\frac{\sinh\alpha_i-\sin\alpha_i}{\cosh\alpha_i+\cos\alpha_i}\right]\left(\sinh\alpha_i X-\sin\alpha_i X\right) \tag{3.25}$$

where α_i constants are calculated using the boundary conditions of Euler-Bernoulli equation. To solve Equation (3.23), the method of variable separation is used and the differential pressure δ_P is separated into a function of *x* and a function of *y*.

$$\delta_P=P_xP_y \tag{3.26}$$

To solve the nonlinear Reynolds' equation these pressure functions can be approximated using polynomials. The expanded functions should satisfy the pressure boundary conditions (Equations (3.20) and (3.21)). The following polynomials have been selected for the pressure functions to satisfy the boundary conditions.

$$P_x = (X-1)(a_1 X^2 + a_2 X^3 + a_3 X^4 + \cdots) \tag{3.27}$$

$$P_y = 1 - 4\beta^2 Y^2 \tag{3.28}$$

The first bracket in Equation (3.27) guaranties the satisfaction of free edge condition at *X=1* and the no flux condition at *X=0*. The P_y is also selected to satisfy the free edge condition at $Y = \pm 1/2\beta$. In order to find the unknown coefficients ($a_1,\ a_2,\ a_3\ \cdots$) in Equation (3.27), P_x and P_y are substituted into Equation (3.23). Since the structural mode shapes are functions of *X* only, the right-hand side of Equation (3.23) is only a function of *X*. However, the left-hand side of Equation (3.23) consists *X* and *Y* terms. In order to find the unknown coefficients ($a_1,\ a_2,\ a_3\ \cdots$), terms that includes *Y* should be eliminated. Hence, the resultant equation is evaluated at *Y = 0* (the mid line of the beam). According to the structural boundary conditions (Equation (3.5)), Φ_i and $\partial\Phi_i/\partial x$ are zero at *X* = 0. Hence, the first two unknown coefficients are determined to be zero. In order to determine the rest of the unknown coefficients ($a_3,\ a_4,\ a_5\ \cdots$), the coefficients of the variables with the same degree should be equal on both sides. The unknown coefficients can be found in terms of structural mode shape amplitudes. The differential pressure distribution can then be found using Equation (3.26). The pressure functions are complex variables. The real parts are in phase with the relative displacement. The force caused by the real part of the pressure acts like a

spring. The imaginary part on the other hand is in phase with the relative velocity and causes a damping force. The imaginary part is larger compared to the real part at low frequencies, however as the working frequency increases the real part increases rapidly. This is due to the fact that at very high frequencies the gas particles cannot escape the gap underneath the beam and they are compressed. This way they act like a spring, absorb and release the energy but do not dissipate it. Figures 3.3 to 3.6 show the real and imaginary part of the first two modes of pressure distribution.

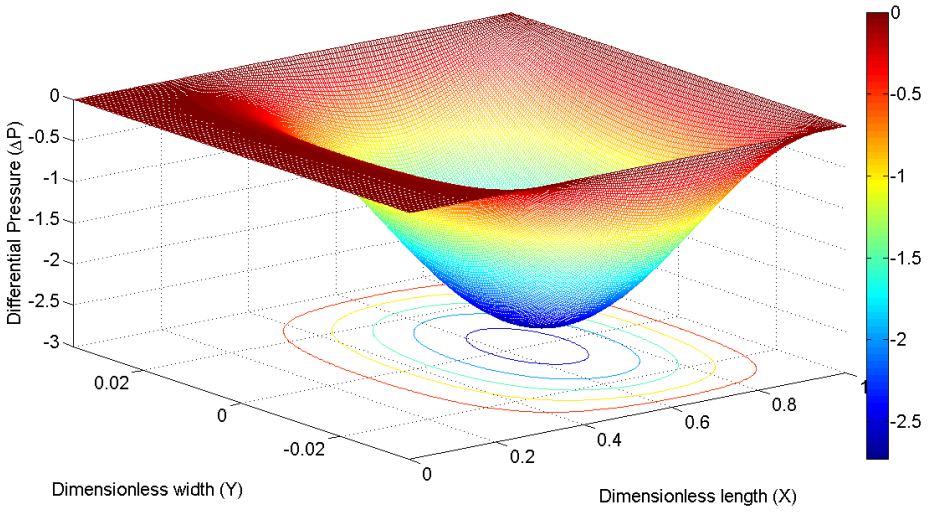

Figure 3.3 Real part of the first mode of the pressure distribution

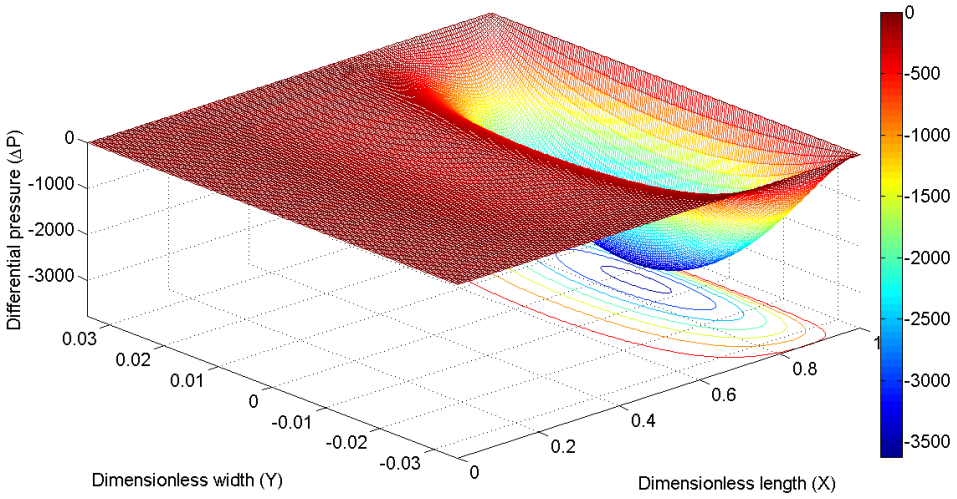

Figure 3.4 Imaginary part of the first mode of the pressure distribution

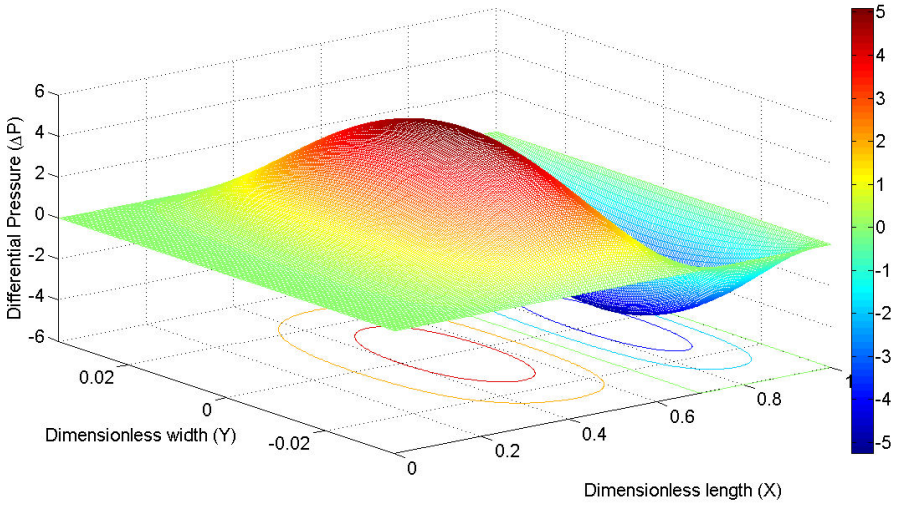

Figure 3.5 Real part of the second mode of the pressure distribution

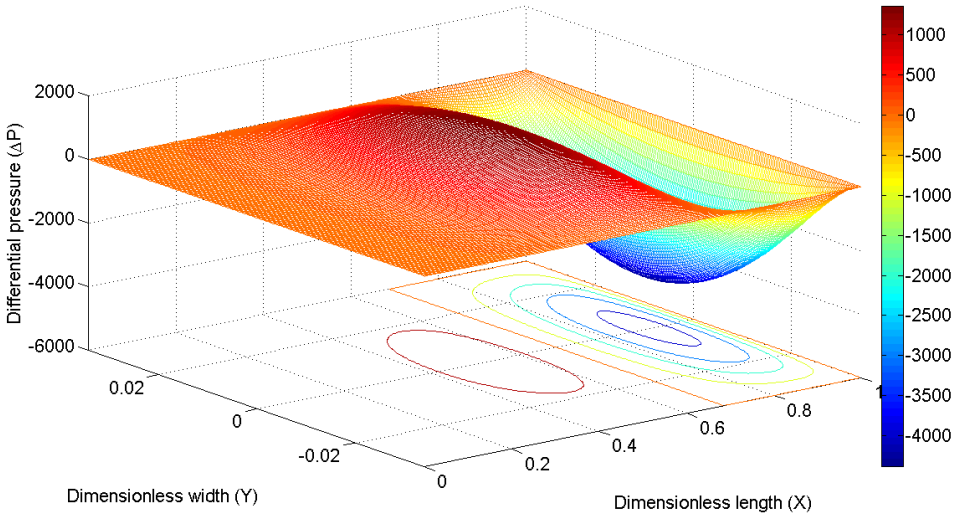

Figure 3.6 Imaginary part of the second mode of the pressure distribution

The pressure distributions can then be integrated over the width of the beam to find the force due to squeeze film damping per unit length.

3.1.1 Squeeze film damping for a perforated beam

The damping factor has a great influence on the performance of a micro system at frequencies close to the natural frequency of the system. Therefore, it is very important to be able to control and optimize the forces due to viscous damping and especially the squeeze film damping. Perforating the vibrating structure is one of the most important and effective methods in controlling the squeeze film damping in MEMS devices. Another method is packaging the structure in rarefied air. Since this sensor is intended to be used as a pressure sensor, this technique cannot be employed. Several techniques have been proposed to model the squeeze film damping for perforated structure [3, 18-20]. In most analyses, a repetitive pattern of holes are considered on the plate with each hole having its

own domain of influence. This individual domain of influence is called a cell. For incompressible flow, Ŝkvor [18] has modeled the flow under each cell by taking ambient pressure boundary condition on the rim of the hole and zero flow rate across each cell. Bao *et al.* [19] have derived a modified Reynolds equation under the assumption of incompressible flow for perforated systems operating at low frequencies considering the friction force in the holes. However, in most cases the investigated structure is considered to be a plate and the density of holes is considered to be high. Hence, the squeeze film force is assumed to be mainly due to the lateral flow to or from the holes. They also assumed that there is no flow into or out of each cell. These assumptions cannot be used for a perforated cantilever beam due to the fact that most of the air below the beam can escape through the side of the beam. To model the squeeze film damping for a perforated beam, the Reynolds' equation has to be modified to consider additional flow through holes. Figure 3.7 shows the control volume under the cantilever beam for a perforated beam and the flow into and out of the control volume.

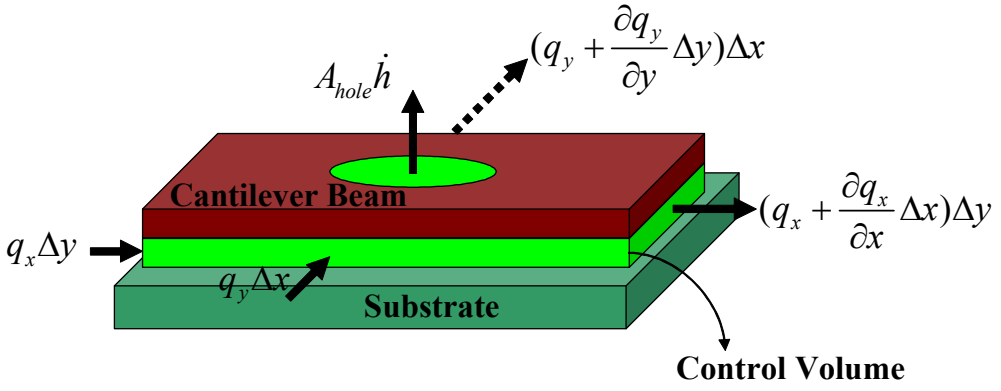

Figure 3.7 Mass flow through rectangular control volume

The friction force applied to the fluid flow though the hole depends on the beam thickness and the hole dimensions. This force can be neglected for thin structures with relatively large

holes. Here we assume the flow through the hole to be frictionless and also the fluid velocity is assumed to be constant over the hole. To develop the modified Reynolds' equation, we start with the continuity equation.

$$-\frac{\partial}{\partial x}\left(\rho q_x\right)\Delta x\Delta y-\frac{\partial}{\partial y}\left(\rho q_y\right)\Delta x\Delta y+\rho Q_z=\frac{\partial}{\partial t}\left(\rho h\right)\Delta x\Delta y \tag{3.29}$$

where Q_z is the volume flow per unit time through the hole. Here we assume that most of the flow escapes through the side of the beam rather than the hole. Hence, the volume flow rate through a hole is considered to be equal to the hole displacement per unit time.

$$Q_z=\rho A_{hole}\dot{h} \tag{3.30}$$

Substituting $q_x=-\frac{h^3}{12\mu}\frac{\partial p}{\partial x}$, $q_y=-\frac{h^3}{12\mu}\frac{\partial p}{\partial y}$ and Q_z into Equation (3.29), the modified Reynolds' equation will have the following form:

$$\frac{\partial}{\partial x}\left(\rho h^3\frac{\partial p}{\partial x}\right)+\frac{\partial}{\partial y}\left(\rho h^3\frac{\partial p}{\partial y}\right)=12\mu\left(\frac{\partial}{\partial t}\left(ph\right)-\rho H_{ratio}\dot{h}\right) \tag{3.31}$$

where the H_{ratio} is defined to be the ratio of the hole area to the area of the beam surface area. Using the dimensionless parameters introduced in Equation (3.16), the dimensionless nonlinear modified Reynolds' equation will be as follows:

$$\frac{\partial^2\delta_P}{\partial X^2}+\frac{\partial^2\delta_P}{\partial Y^2}-\sigma\frac{\partial\delta_P}{\partial T}=\sigma\frac{\partial\delta_R}{\partial T}\left(1-H_{ratio}\right) \tag{3.32}$$

To solve this equation the same technique that used for Reynolds' equation is used. However, it should be considered that "the area moment of inertia" and "the cross sectional area" of the beam vary along the length of the beam. In order to avoid difficulties of using Equation(3.1), the effective values of the above mentioned parameters are used in Equation (3.1).

3.1.2 The Effect of Initial Curling on the Squeeze Film Damping

In the previous sections the cantilever beam is assumed to be flat initially. However, initial curling can happen due to the stress gradients within the cantilever layer and fabrication issues such as stiction. If a cantilever beam is curled, either up or down, the initial air film thickness varies along the x axes (Figure 3.8). The air gap height has a great influence on the squeeze film force. Hence, the air gap variation should be taken into account in squeeze film damping calculation. For a uniformly distributed stress gradient, the initial curling can be assumed to have a quadratic form. Measuring the air gap height at different positions, the shape of the cantilever beam can be fitted to a function of the following form:

$$h(x) = h_0\left[1+\varepsilon\left(\frac{x}{l}\right)^2\right] \tag{3.33}$$

where h_0 is the gap height at the anchor and ε is the shape factor which is positive for a beam that is curled up, and negative for a beam that is curled down.

Figure 3.8 Initially curled cantilever beam due to the stress gradients within the cantilever layer and fabrication issues such as stiction

As mentioned before, the gap height for a deflected beam will have the following form:

$$h_{deformed} = h(x) + \delta_r(x) = h_0\left[1 + \varepsilon\left(\frac{x}{l}\right)^2\right] + \delta_r(x) \tag{3.34}$$

This can be changed into a non-dimensional form using parameters introduced in Equation (3.16):

$$H_{deformed} = \frac{h_{deformed}}{h_0} = 1 + \varepsilon X^2 + \delta_R(X) \tag{3.35}$$

Substituting the above equation into Equation (3.17) the Reynolds' equation will have the following form.

$$\frac{\partial}{\partial X}\left(\left(1+\delta_P\right)\left(1+\varepsilon X^2+\delta_R\right)^3\frac{\partial \delta_P}{\partial X}\right)+\frac{\partial}{\partial Y}\left(\left(1+\delta_P\right)\left(1+\varepsilon X^2+\delta_R\right)^3\frac{\partial \delta_P}{\partial Y}\right)= \sigma\frac{\partial}{\partial T}\left(\left(1+\delta_P\right)\left(1+\varepsilon X^2+\delta_R\right)\right) \tag{3.36}$$

Expanding the above equation and assuming δ_R, δ_P and ε to be smaller than 1, the Reynolds' equation will be as follows:

$$6\varepsilon X\frac{\partial \delta_P}{\partial X}+\left(1+3\varepsilon X^2\right)\left(\frac{\partial^2 \delta_P}{\partial X^2}+\frac{\partial^2 \delta_P}{\partial X^2}\right)-\sigma\left(1+\varepsilon X^2\right)\frac{\partial \delta_P}{\partial T}=\sigma\frac{\partial \delta_R}{\partial T} \tag{3.37}$$

For perforated beams the above equation will have the following form

$$6\varepsilon X\frac{\partial \delta_P}{\partial X}+\left(1+3\varepsilon X^2\right)\left(\frac{\partial^2 \delta_P}{\partial X^2}+\frac{\partial^2 \delta_P}{\partial X^2}\right)-\sigma\left(1+\varepsilon X^2\right)\frac{\partial \delta_P}{\partial T}=\sigma\left(1-H_{ratio}\right)\frac{\partial \delta_R}{\partial T} \tag{3.38}$$

For ε equal zero the above equations are reduced to Equations (3.19) and (3.32).

To solve this equation harmonic functions are considered for δ_R and δ_P and will use the method of variable separation to solve the linear partial differential equation. Since, the boundary conditions have not been changed for this problem the same polynomials can be used here again (Equations (3.27) and (3.28)).

3.2 Air flow damping

The air flow damping is the other type of viscous damping force that affects the beam's motion. This damping mechanism is caused by the airflow surrounding the beam in the free space. The airflow around the beam can be described using the continuity Equation (3.39) and the Navier-Stokes (3.40) Equation.

$$\nabla \vec{V}(x,y,z) = 0 \tag{3.39}$$

$$-\nabla p = -\mu \Delta \vec{V} + \rho_{air}(\vec{V}.\nabla)\vec{V} + \rho_{air}\frac{\partial \vec{V}}{\partial t} \tag{3.40}$$

where $\vec{V}(x,y,z)$ is the velocity vector of the air particles at each point. The boundary conditions for the above equations are as follows:

$$\text{at infinity: } \vec{V} = 0,\ p = p_a \tag{3.41}$$

$$\text{on the beam surface: } \quad \vec{V}(x,y,z) = \begin{bmatrix} 0 & 0 & \dfrac{\partial z(x,t)}{\partial t} \end{bmatrix} \tag{3.42}$$

Since the Reynolds' number is very small (Re<<1), the second term on the right-hand side of Equation (3.40) can be neglected compared to the first term which leads to the Stokes equation [21].

$$-\nabla p = -\mu \Delta \vec{V} + \rho_{air} \frac{\partial \vec{V}}{\partial t} \tag{3.43}$$

As previously stated by *Hosaka et al.* [21-23] the Stokes equation cannot be solved analytically for a vibrating micro beam geometry. Therefore a closed form solution cannot be obtained. For a thin beam at very small Reynolds' numbers, the streamlines of a flow around a beam are similar to that of a sphere. The flow patterns around a beam and a sphere are shown in Figure 3.9.

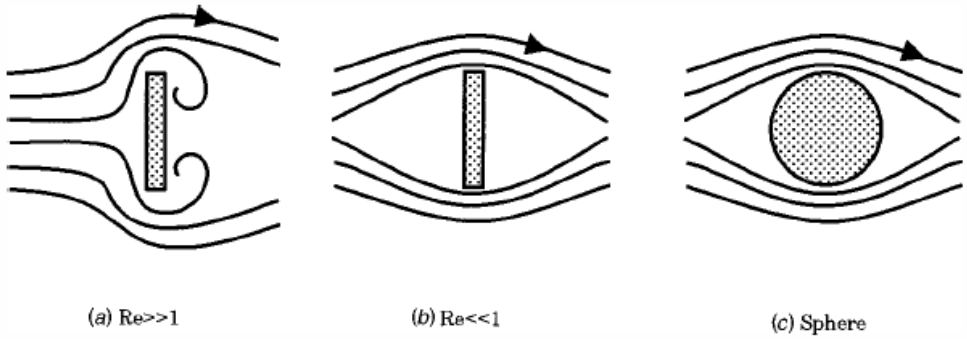

Figure 3.9 Flow pattern around a beam and a sphere [23]

Since the flow pattern is similar for a beam (for $Re << 1$) and a sphere, the space derivatives of $\vec{V}$ in Equations (3.39) and (3.43) are of the same order of magnitude. Hence, the order of magnitude of the fluid force, which is given by pressure (p) and the gradient of $\vec{V}$, are the same [21-23]. Since, Equations (3.39) and (3.43) are linear, the flow around the beam can be found using the superposition principle and the beam can be substituted with a series of spheres of the same width.

.

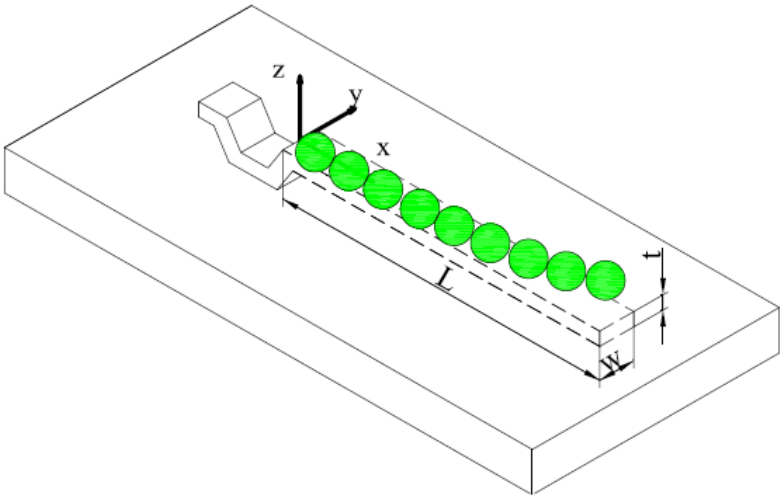

Figure 3.10 A cantilever beam substituted with a series of spheres

Substituting the beam with a string of spheres, Hosaka *et al* [21-23], presented an approximate solution for the micro beam geometry known as the *bead model*. The fluid force applied to an oscillating sphere has the following form:

$$F = -\beta_1 \frac{\partial z(x,t)}{\partial t} - \beta_2 \frac{\partial^2 z(x,t)}{\partial t^2} \tag{3.44}$$

where

$$\beta_1 = 3\pi\mu b + \frac{3}{4}\pi b^2 \left(2\rho_{air}\mu\omega\right)^{1/2}$$

$$\beta_2 = \frac{1}{12}\pi\rho_{air} b^3 + \frac{3}{4}\pi b^2 \left(\frac{2\rho_{air}\mu}{\omega}\right)^{1/2}$$

The first term in Equation (3.44) is the damping force and the second one is the additional mass. The second term is very small and can be neglected. Equation (3.44) represents the

force that is applied to a sphere with velocity of $\frac{\partial z}{\partial t}$. Neglecting the flow interaction among spheres, the air velocity at the contact point of two spheres is $2\frac{\partial z}{\partial t}$. The air velocity at the surface of a sphere equals the sphere velocity. Hence, when a string of spheres is oscillating at a velocity of $\frac{\partial z}{\partial t}$, the airflow force of $\frac{F}{2}$ is applied to each sphere and the force per unit length applied to the cantilever beam is given by [3]

$$f_{airflow} = \frac{F}{2b} = -\left(\frac{3}{2}\pi\mu + \frac{3}{8}\pi b\sqrt{2\rho_{air}\mu\omega}\right)\frac{\partial z(x,t)}{\partial t} \tag{3.45}$$

Substituting Equation (3.3) into Equation (3.45), the airflow force can be rewritten in the form of relative displacement.

$$f_{airflow} = C_a\left[\frac{\partial \delta_r(x,t)}{\partial t} + \frac{\partial\left(Z_0 e^{i\omega t}\right)}{\partial t}\right] \tag{3.46}$$

where C_a is the airflow damping coefficient and can be expressed as follows [3]:

$$C_a = \frac{3}{2}\pi\mu + \frac{3}{8}\pi b\sqrt{2\rho_{air}\mu\omega} \tag{3.47}$$

3.3 Frequency Response Calculation

In order to find the frequency response of the cantilever beam the squeeze film damping and the airflow damping forces have to be substituted into Equation (3.4) . Since, the squeeze film damping is in non-dimension form, the Euler-Bernoulli equation has to be changed into dimensionless form. Using the same parameters introduced in Equation (3.16), the Euler-Bernoulli equation can be changed into non dimension form.

$$\frac{\partial^4 \delta_R}{\partial X^4} + \frac{\rho A_{eff} \omega^2 l^4}{EI_{eff}} \frac{\partial^2 \delta_R}{\partial T^2} = \frac{p_{air} b l^4}{EI_{eff} h_0} \left(F_{airflow} + F_{squeeze} + \frac{Z_0 \rho A_{eff} \omega^2}{p_{air} b} e^{iT} \right) \tag{3.48}$$

where the dimensionless airflow force has the following form:

$$F_{airflow} = -C_a \frac{\omega}{p_a b} \left(h_0 \frac{\partial \delta_R}{\partial T} + i Z_0 e^{iT} \right) \tag{3.49}$$

The squeeze film damping for a solid beam is:

$$F_{squeeze} = \beta \int_{-\frac{1}{2\beta}}^{\frac{1}{2\beta}} (\delta_P) dY = \frac{2}{3} P_X \tag{3.50}$$

However, for a perforated beam the squeeze force per unit length at each section can be found as follows:

$$F_{squeeze} = 2\beta \int_{a}^{\frac{1}{2\beta}} (\delta_P)\, dY \tag{3.51}$$

where *a* is zero at a section without a hole and it is equal to $\frac{d}{2}$ (half of the hole width) at a section that a hole exists.

Substituting the relative displacement with a harmonic function ($\delta_R = \overline{\delta_R} e^{iT}$) and expanding $\overline{\delta_R}$ using the structural mode shapes, the equation of motion of the system will have the following form:

$$\frac{\partial^4 \sum A_i \Phi_i}{\partial X^4} - C_1 \omega^2 \sum A_i \Phi_i = C_2 \left(-iC_a \frac{\omega h_0}{p_a b} \sum A_i \Phi_i + \sum A_i F_{squeeze}\Big|_i + \frac{Z_0 \rho A_{eff} \omega^2}{p_{air} b} - iC_a \frac{\omega Z_0}{p_a b} \right) \tag{3.52}$$

where $C_1 = \frac{\rho A_{eff} l^4}{E I_{eff}}$ and $C_2 = \frac{p_a b l^4}{E I h_0}$

Multiplying Equation (3.52) by Φ_j and integrating the resultant expression over the length of the beam, the mode shape amplitudes can be calculated using Equation(3.53).

$$\begin{Bmatrix} A_1 \\ \vdots \\ A_n \end{Bmatrix} = \begin{bmatrix} \alpha_i{}^4 - C_1\omega^2 + iC_2C_a\dfrac{\omega h_0}{P_a b} - C_2\displaystyle\int_0^1 \Phi_1 F_{squeeze}\big|_i \, dX & \cdots & -C_2\displaystyle\int_0^1 \Phi_1 F_{squeeze}\big|_n \, dX \\ \vdots & \ddots & \\ -C_2\displaystyle\int_0^1 \Phi_n F_{squeeze}\big|_i \, dX & & \alpha_n{}^4 - C_1\omega^2 + iC_2C_a\dfrac{\omega h_0}{P_a b} - C_2\displaystyle\int_0^1 \Phi_n F_{squeeze}\big|_n \, dX \end{bmatrix}^{-1}$$
$$\times \begin{Bmatrix} \dfrac{C_2 Z_0}{p_a b}\left(\rho A_{eff}\omega^2 - iC_a\omega\right)\displaystyle\int_0^1 \Phi_1 dX \\ \\ \dfrac{C_2 Z_0}{p_a b}\left(\rho A_{eff}\omega^2 - iC_a\omega\right)\displaystyle\int_0^1 \Phi_1 dX \end{Bmatrix}$$

(3.53)

where $\alpha_n{}^4 = \int_0^1 \Phi_n \dfrac{\partial^4 \Phi_n}{\partial X^4} dX$

To find the frequency response of the beam, the mode shape amplitudes, A_i, are divided by the base oscillation amplitude Z_0 and the frequency response is as follows:

$$\delta_R = \sum\left(A_i \frac{h_0}{Z_0} \Phi_i \right) \tag{3.54}$$

As we can see from Equation (3.53), the air flow damping contributes to the diagonal terms only. However the squeeze film damping contributes to both the diagonal and off-diagonal terms. The diagonal terms are the coefficients of each mode and the off-diagonal terms represent the *cross-talk* coefficients between modes [24]. Neglecting the off-diagonal terms Equation (3.53) can be re-arranged into the following form:

$$\begin{Bmatrix} A_1 \\ \vdots \\ A_n \end{Bmatrix} = \begin{bmatrix} \dfrac{1}{(1+k_1)+2\zeta_1\left(\dfrac{\omega}{\omega_1}\right)-\left(\dfrac{\omega}{\omega_1}\right)^2} & & \\ & \ddots & \\ & & \dfrac{1}{(1+k_n)+2\zeta_n\left(\dfrac{\omega}{\omega_n}\right)-\left(\dfrac{\omega}{\omega_n}\right)^2} \end{bmatrix} \times \begin{Bmatrix} \dfrac{Z_0}{h_0}\left(\left(\dfrac{\omega}{\omega_1}\right)^2 - i\dfrac{l^4}{{\alpha_1}^4 EI_{eff}}\omega\right)\displaystyle\int_0^1 \Phi_1 dX \\ \\ \dfrac{Z_0}{h_0}\left(\left(\dfrac{\omega}{\omega_n}\right)^2 - i\dfrac{l^4}{{\alpha_n}^4 EI_{eff}}\omega\right)\displaystyle\int_0^1 \Phi_n dX \end{Bmatrix} \tag{3.55}$$

The total damping factor for each mode can be found using the following equation:

$$\zeta_i = \frac{1}{2{\alpha_i}^4}\left[C_2 C_a \frac{\omega h_0}{P_a b} - C_2 \int_0^1 \Phi_i imag\left(F_{squeeze}\Big|_i\right) dX\right]\left(\frac{\omega_n}{\omega}\right) \tag{3.56}$$

and the spring factor due to squeeze film can be calculated as follows:

$$k_i = \frac{1}{{\alpha_i}^4}\left[-C_2 \int_0^1 \Phi_i real\left(F_{squeeze}\Big|_i\right) dX\right] \tag{3.57}$$

3.4 Model Results

In this section numerical results for different cantilever beams are presented using the mechanical theory developed in the previous sections. The magnitude of the frequency response and the viscous damping behavior (airflow and squeeze film) of different beams are presented to help gain a better understanding of the system performance. The model results that are presented here are obtained using the first two modes of the system. The effect of higher mode shapes can be shown to be negligible at low frequency region.

Table 3.1Material Properties used in numerical calculations

Parameter	**Value**	**Reference**
Silicon Nitride Young's Modulus	238 GPa	[3]
Silicon Nitride Density	2865 kg/m^3	[3]
Polysilicon (PolyMUMPs) Young's Modulus	158 GPa	[25]
Polysilicon (PolyMUMPs) Density	2330 kg/m^3	[25]
Air Viscosity	1.8×10^{-5} N.s/m^2	[15]
Air Density	1.3 kg/m^3	[15]

Table 3.1 presents the material constants used in this analysis. The thin film properties depend on different parameters especially the deposition process. In addition to these parameters, the air gap and the thickness of each set of cantilever beams are presented in tables 3.2 and 3.3. The first sets of beams are fabricated using a process developed at Microfabrication Lab. at Northeastern University [3]. The second sets of the cantilever beams are fabricated using PolyMUMPs process. The Poly2 layer is used to fabricate these beams.

Table 3.2 Silicon nitride cantilever beam dimensions

Parameter	**Value**
Length	120 μm
Width	10 μm
Nitride Thickness	0.45 μm
Number of Holes	12
Hole size	4 μm
Air gap at anchor	2 μm
Epsilon	0.2

Table 3.3 Polysilicon cantilever beam dimensions

Parameter	**Value**
Length	270 μm
Width	10 μm
Nitride Thickness	1.5 μm
Number of Holes	12
Hole size	4 μm
Air gap at anchor	2.75 μm
Epsilon	-0.14

Frequency response and the viscous damping of silicon nitride beam solid and perforated beam is shown in figure 3.11, 3.12. As expected the damping factor for a perforated beam is lower than a solid beam. This causes the magnitude of the frequency response of the perforated beam to be larger than a solid beam at frequencies close to the natural frequency.

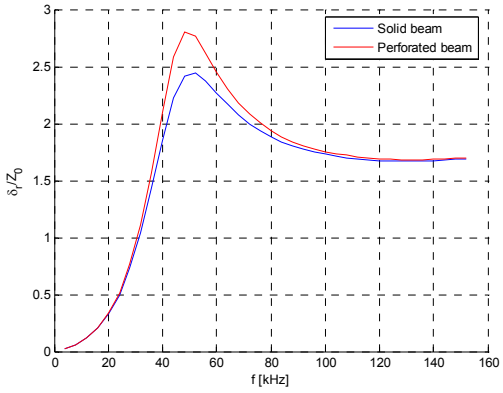

Figure 3.11 Frequency response of a solid and perforated beam

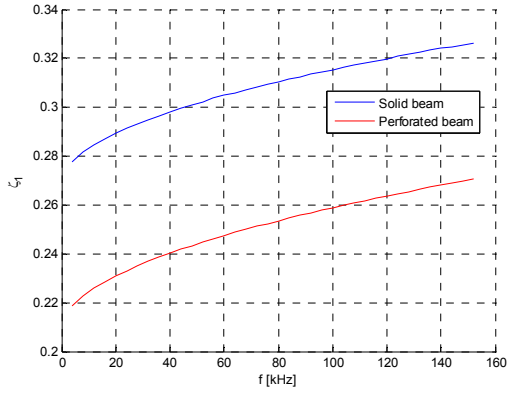

Figure 3.12 Total viscous damping factor of a solid and perforated beam

Figure 3.13, 3.14 show the frequency response and the damping factor of a cantilever beam fabricated with the PolyMUMPs process. Although, the length of this beam is longer than the nitride beam it has a higher frequency response due to its thickness. The difference between the damping factor of a solid and a perforated beam is less which is due to a larger gap height.

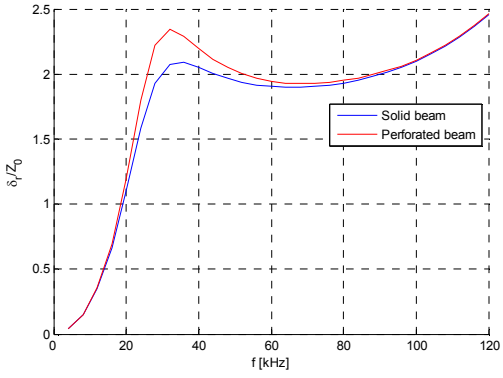

Figure 3.13 Frequency response of a solid and perforated beam

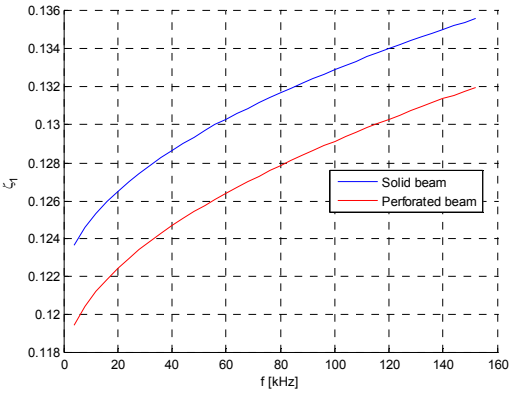

Figure 3.14 Total viscous damping factor of a solid and perforated beam

3.5 Pressure Sensor

The mechanical behavior of a cantilever beam operating in air is highly depended on the damping forces. For the micro device under investigation, squeeze film damping and air flow damping are the two damping mechanisms that act on the structure. The effect of damping becomes more dominant at frequencies close to the natural frequency. Figure 3.15 shows the effect of pressure on the device frequency response.

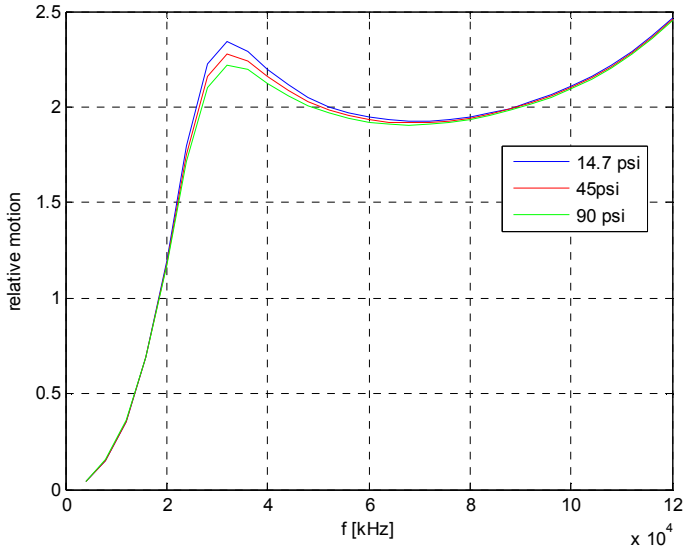

Figure 3.15 Frequency response for different pressure values

This dependency (at frequencies close to the fundamental frequency) can be used to measure quantities that can affect the system damping factor. Between the two damping mechanisms, squeeze film damping is a function of viscosity only, while the air flow damping varies with both viscosity and air density. Air viscosity can be expressed as a function of temperature only. The air viscosity relationship with temperature and pressure can be investigated using Equation (3.58) .

$$\mu_{air} = 0.0170257 + 6.05434e-5T + 1.332e-7T^2 + 8.08321e-7P + 5.97259e-10P^2 \quad (3.58)$$

where T is temperature in degrees Celsius. P is the absolute pressure in *psi* and μ_{air} is the air viscosity given in centipoises (*cp*) [3]. However, the air density is a function of both pressure and temperature and can be modeled using the ideal gas law.

$$\rho_{air} = \frac{P}{RT[^{o}K]} \quad (3.59)$$

where $R=287.05\ [J/kg^{o}K]$ is the gas constant for dry air, P is the pressure in Pascals and T is the temperature in degrees Kelvin. Knowing this we can conclude that the air flow damping is a function of both pressure and temperature while squeeze film damping changes only with temperature. This is shown in Figures 3.15, 3.16 using the model to predict the squeeze film damping factor and the airflow damping factor.

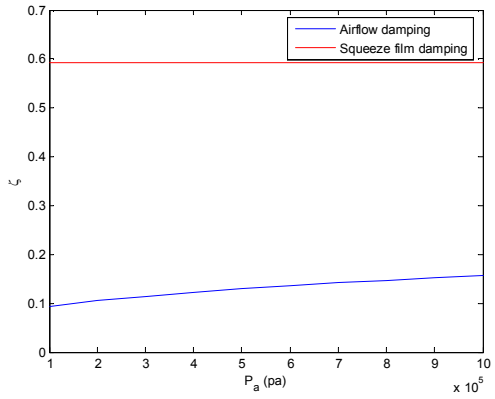

Figure 3.16 Airflow damping and squeeze film damping versus ambient pressure

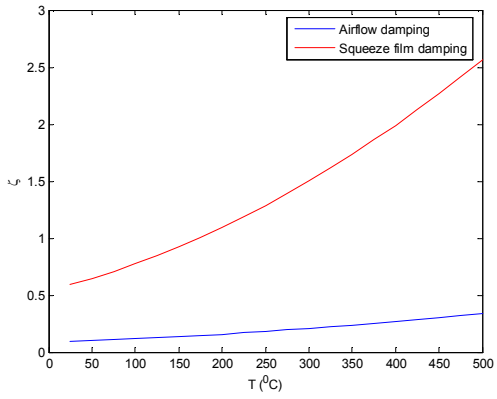

Figure 3.17 Airflow damping and squeeze film damping versus ambient temperature

The squeeze film damping increases when the gap height is decreasing. At very narrow gaps it is the squeeze film damping that governs the frequency response of the beam.

However, as the gap height increases, the squeeze film damping decreases and the effect of airflow damping on the beam frequency response becomes more visible. As it is mentioned the airflow damping is a function of both pressure and temperature, therefore, for a cantilever beam with large gap height, the frequency response of the system can be affected by both pressure and temperature. Hence, running a cantilever beam at a known frequency, displacement and temperature, gives us enough information to determine pressure. To measure the air pressure, sensor's frequency response has to be measured at different pressures. Then, the pressure can be measured by running the beam at a specific frequency close to the natural frequency of the system and compare the measured displacement to the measured frequency responses at different pressures.

Chapter 4
Optical Readout

In chapter two the relative displacement of the cantilever beam with respect to the substrate (gap height) was related to the substrate excitation using vibration theory. It was also shown that the frequency response of the device and the damping factor depend on the ambient pressure and temperature. To be able to sense pressure, using the proposed sensor, the relative motion (gap height) is measured.

An optical interferometric technique has been used to measure the gap height. The free standing cantilever beam and the substrate are two parallel mirrors. These two mirrors, free standing cantilever beam and its substrate, correspond to a Fabry-Perot in reflectance. The power reflectance is the fraction of the intensity of light being reflected from the Fabry-Perot structure [3]. Interference between multiple reflections causes the power reflectance of the received signal to be a function of the cavity's optical path length [26].

In modeling the Fabry-Perot spectra, the two mirrors are assumed to be flat and parallel. For more details in the interferometric analysis used for the MEMS Fabry-Perot device, refer to [3]. Two different sets of devices have been used in this work. The first set was fabricated in the Microfabrication Laboratory of Northeastern University, Boston, USA. These devices were fabricated on a silicon substrate and the free standing cantilever beam is fabricated out of silicon nitride. The second set of devices was fabricated at MEMSCAP facilities using the PolyMUMPs process. The moving mirrors of these devices are made of a 1.5 micron polysilicon layer.

The objective of this chapter is to find a relation between the power reflectance of the received signal and the air gap size. The general theory of multilayer films is presented in Appendix A. In this chapter this theory is applied to the problem at hand.

4.1 Optical Transfer Function

For the system under investigation, the wavelength of the laser is constant and the thickness and the index of refraction of each layer is constant except for the air gap. By calculating the power reflectance for different values of gap height, the transfer matrix of the optical system can be found.

The power reflectance is calculated for the two cases of nitride cantilever beams and the cantilever beams that were fabricated using PolyMUMPs. Tables 4.1 and 4.2 show the index of refraction for each layer.

Table 4.1 Refractive index of the materials used in PolyMUMPs

	Refractive Index	**Reference**
Air	1	[3]
Silicone Nitride	2.19	[27]
Polysilicon	4	[27]
Silicon (substrate)	$3.8411 + i0.0167$	[3]

Table 4.2 Refractive index of the materials used in Nitride device

	Refractive Index	**Reference**
Air	1	
Silicone Nitride	2.0737	[3]
Silicon (substrate)	$3.8411 + i0.0167$	[3]

The optical transfer functions of the two systems are shown in figures 4.1 to 4.3. The vertical blue line indicates the operating point of the system. Figure 4.1 corresponds to the device fabricated using the poly1 layer. The thickness of the cantilever beam is $2\mu m$ and the

gap height is $2\mu m$. Figure 4.2 shows the transfer function of a cantilever beam using the poly2 layer. The thickness of the cantilever beam is $1.5\mu m$ and the gap height is $2.75\mu m$.

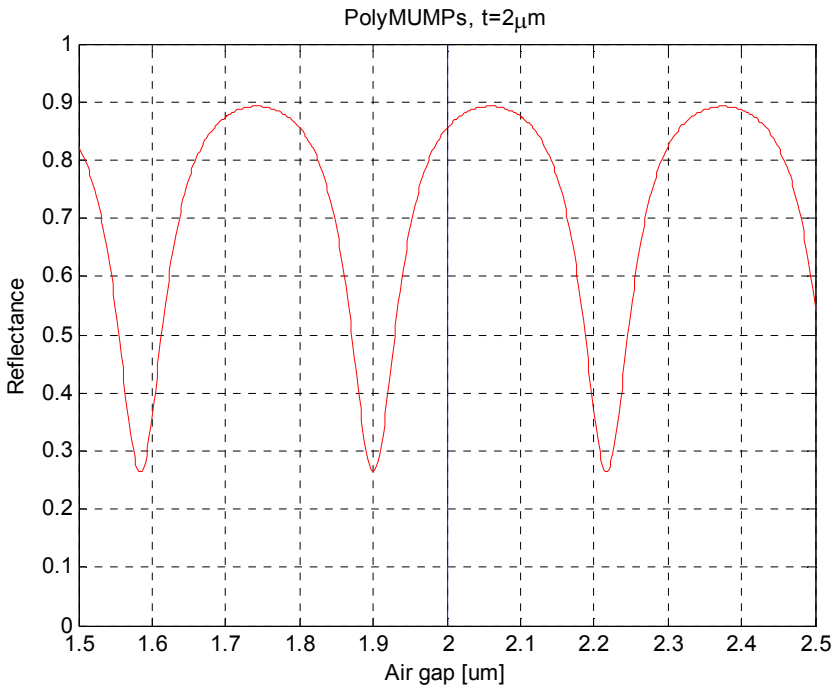

Figure 4.1 Optical transfer function for a PolyMUMPs device with the Poly1 layer

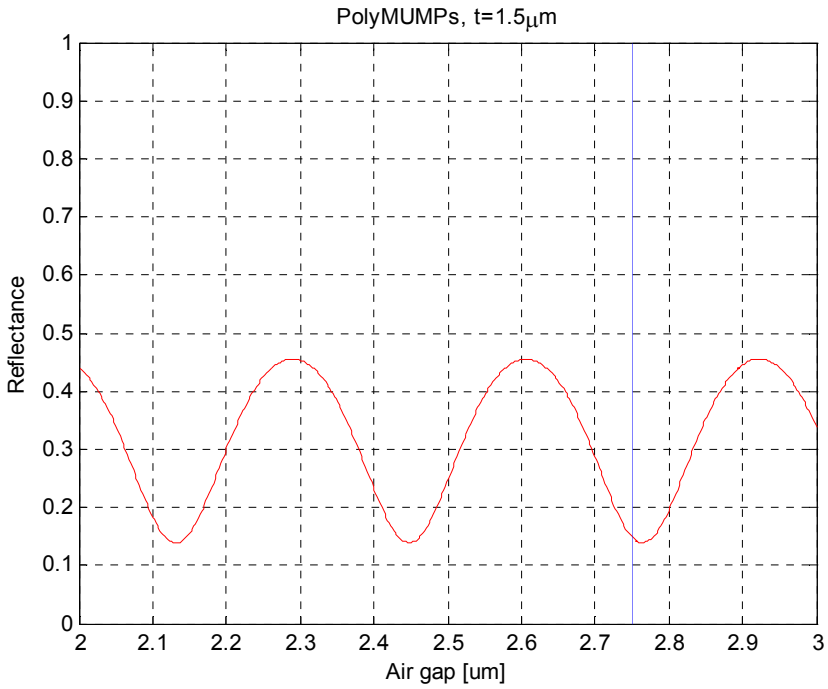

Figure 4.2 Optical transfer function for a PolyMUMPs device with the Poly2 layer

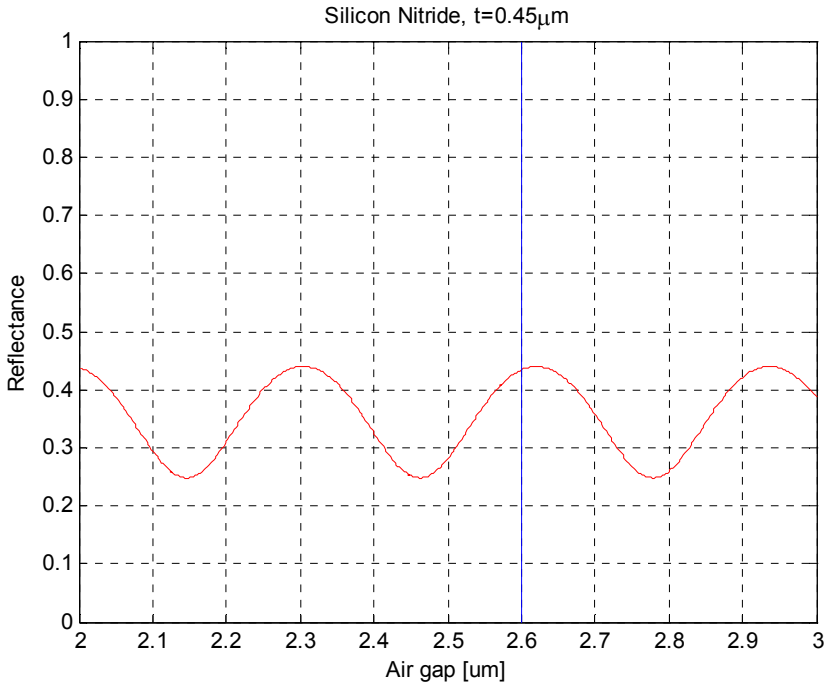

Figure 4.3 Optical transfer function for a Silicon Nitride

The transfer function of this system is a harmonic function with its period equal to $\frac{\lambda}{2}$. As we can see at certain gap heights the reflectance spectrum coming from the Fabry-Perot structure is at its minimum value. This phenomenon is called a destructive interference. On the other hand for some gap heights the reflectance spectrum is at its peak. This interference is called constructive.

The displacement sensitivity of the reflectance curve is the slope of this curve ($\frac{\partial R}{\partial h}$). It is important to select the initial gap height to get the maximum sensitivity. For the devices that are fabricated with PolyMUMPs process, as we can see in Figure 4.1 and Figure 4.2, the initial gap height is either close to a peak or a dip. At these points the displacement sensitivity is close to zero. Unfortunately, due to fixed thicknesses that are provided by PolyMUMPs, the initial gap height cannot be optimized to have the maximum sensitivity. As it was discussed in chapter 2, the cantilever beams may bend up or down after release. This curling causes the initial gap height to vary along the length of the beam which can be used to our advantage. By moving the laser spot location on the beam toward the tip or the root of the beam a point can be found that has the best sensitivity for a released beam. This way we can compensate for the fixed gap that is offered by the PolyMUMPs process.

4.2 Cantilever Beam Optical Response

To get the optical signal of the cantilever beam, the thickness of air gap has to be substituted by the initial gap height plus the relative motion of the beam with respect to the substrate [3].

$$l_{air} = h_0 + \delta_r e^{i\omega t} \tag{4.1}$$

Substituting the above equation in the transfer matrix that corresponds to air, the matrix will have the following form [3]:

$$M_{air} = \begin{bmatrix} \cos k_{air}(h_0 + \delta_r e^{i\omega t}) & \frac{-i}{n_{air}} \sin k_{air}(h_0 + \delta_r e^{i\omega t}) \\ -in_{air} \sin k_{air}(h_0 + \delta_r e^{i\omega t}) & \cos k_{air}(h_0 + \delta_r e^{i\omega t}) \end{bmatrix} \tag{4.2}$$

Using the above transfer matrix the power reflectance can be calculated for different values of the relative motion amplitudes. The cantilever beam transfer function and the interferometric optical response for PolyMUMPs and nitride devices are presented in figures 4.4 to 4.6. The interferometric optical signal corresponds to the signal observed at the oscilloscope during operation.

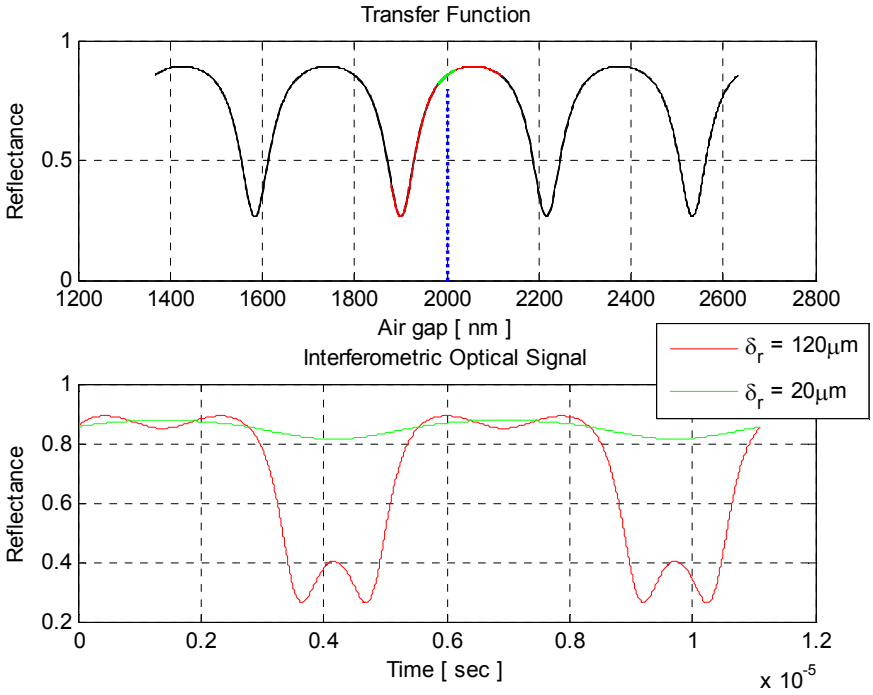

Figure 4.4 Interferometric optical signal for the PolyMUMPs device with the Poly1

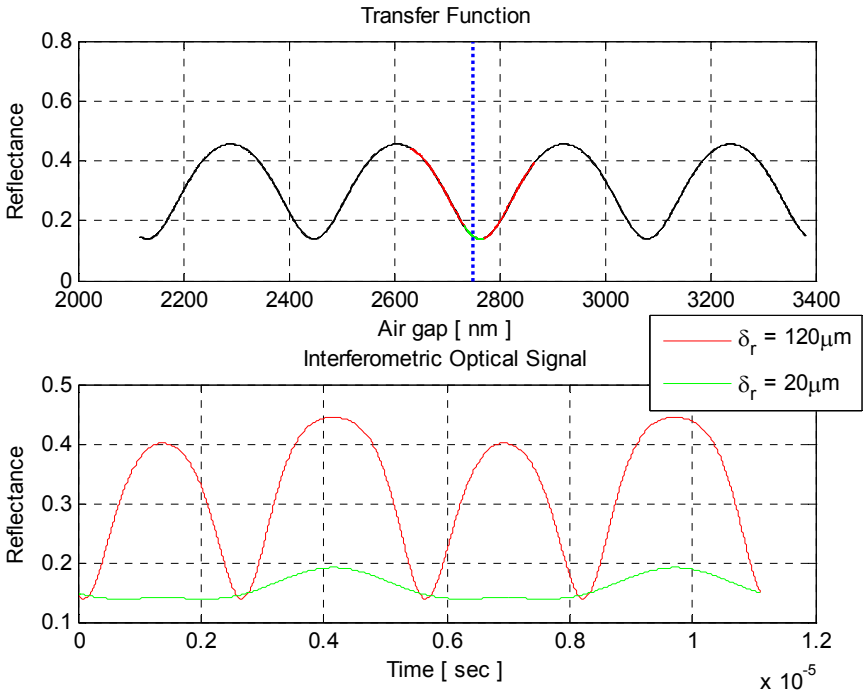

Figure 4.5 Interferometric optical signal for the PolyMUMPs device with the Poly2

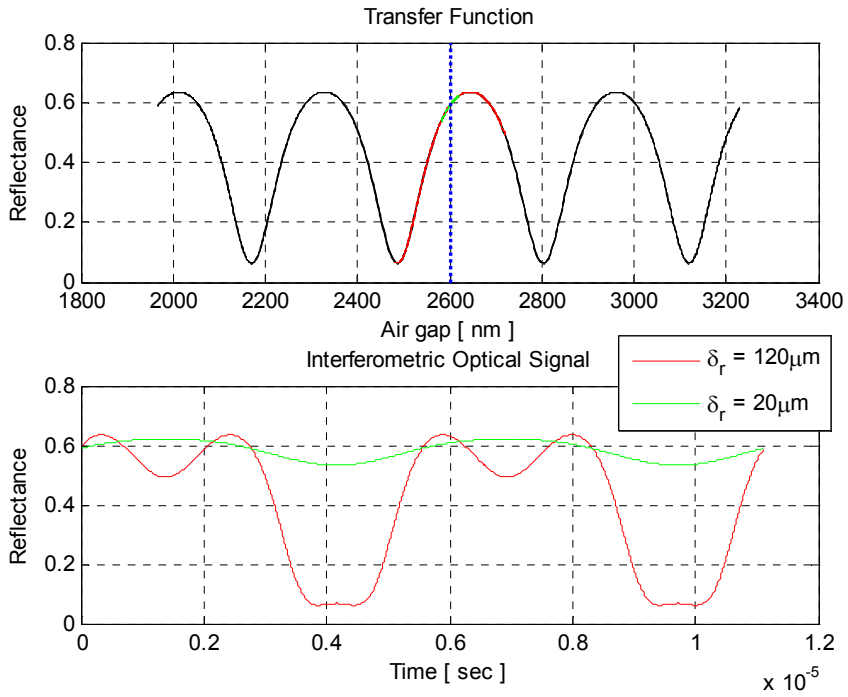

Figure 4.6 Interferometric optical signal for the Silicon Nitride device

Figures 4.4 to 4.6 show both the graph of the optical transfer function and the interferometric optical signal for different cantilever beams. The optical parameters that are used to calculate the above figures are presented in tables 4.1 and 4.2. The blue dotted line indicates the initial gap height (the operating point of the device). When the beam starts to move harmonically with specific amplitude, the reflectance starts oscillating around the operating point. The reflectance corresponding to that motion is plotted as a function of time in the bottom figures. The form of this signal depends on how linear the optical transfer function is around the operation point. Increasing the motion amplitude, the interferometric signal starts to deform and lobes start to appear. The lobes in the interferometric signal appear because the reflectance is changing from a maximum to a minimum and back again.

This non-linear interferometric optical signal describes a total displacement greater than $\frac{\lambda}{4}$, (greater than half a period of the transfer function). The AC component of this signal is used for optical system calibration. Due to its non-linearity, this optical calibration signal can be uniquely fitted to the AC component of the interferometric optical signal measured from an oscilloscope. The parameters obtained from the fitting process can be used to obtain the optical transfer function which can be used to find the air gap height. The Matlab code which performs the fitting process is presented in Appendix 2.

Chapter 5
Test Structures and Mechanical Electro-Optical Test System

To measure the frequency response of the cantilever beams and the air pressure a mechanical electro-optical test system was setup. Specifications and the working principles of the test system are described in this chapter.

The test system can be divided into two major components; the mechanical excitation system, responsible for generating substrate displacement excitation and the electro-optical system, which measures the optical response of the cantilever beam. The mechanical system excites the substrate at a preset frequency by applying a sinusoidal signal with small amplitude. At the same time, a laser beam is focused on the excited cantilever beam. The reflected optical signal is then detected and measured using the electro-optical system. The relative deflection of the cantilever beam with respect to the substrate is determined by processing the electrical signal using a Matlab® code. This cycle is performed at various frequencies and it is used to determine the frequency response of the cantilever beam. Frequencies up to 140 kHz have been used for the tests. Specifications, layout and calibration of the mechanical excitation system and the electro-optical system are described in detail in the following sections.

5.1 Mechanical System

The mechanical excitation system consists of three components: a piezoelectric actuation system manufactured by PI (Physik Instrumente) L.P.[1], which generates the mechanical excitation, a custom made pressure chamber used to provide a pressurized environment and a Laser Doppler Vibrometer (LDV) manufactured by Polytech, Inc.[2], which is used for calibrating the mechanical excitation system by measuring the substrate displacement. Figure 5.1 shows a test chip mounted on the piezoelectric actuator. The piezo actuator is fixed to the pressure chamber using nail polish. Double sided tape could not be used since the opeartying point of the system is changed as the tape is squeezed at high pressures.

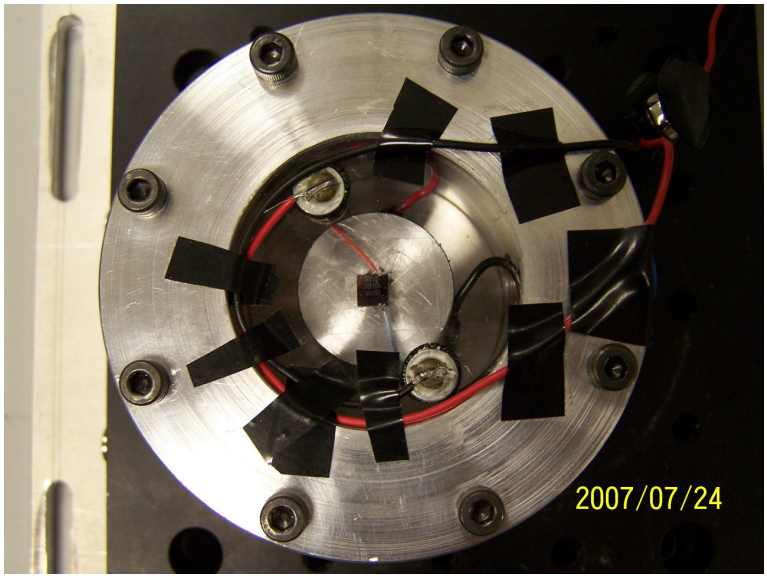

Figure 5.1 Test Chip mounted on a piezoelectric actuator in the pressure chamber

[1] PI (Physik Instrumente) L.P., Auburn, MA, USA
[2] Polytec, Inc., Tustin, CA, USA

A function generator generates the excitation signal which is then amplified by a power amplifier. The amplified excitation signal drives the piezoelectric actuator, resulting in a small displacement of the test chip ($10-20nm$) and therefore, excites the cantilever beam. The LDV system is shown in figure 5.2. As noted earlier, an LDV is used to calibrate the mechanical excitation system by measuring displacement of substrate within the range of applied frequencies. To calibrate the mechanical system, a constant substrate displacement is aimed by adjusting the input voltage to the piezoelectric actuator.

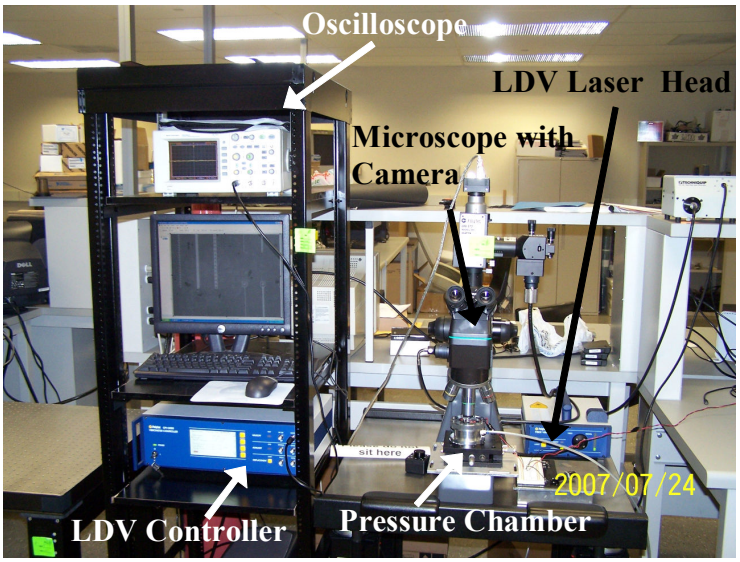

Figure 5.2 Laser Doppler Vibrometer setup

Components of the piezoelectric actuation system and LDV setup are described in detail in the subsequent sections. The piezoelectric actuation system consists of four main parts, the test chip, the actuator, the pressure chamber and the excitation signal. Details of each component are explained in the following sections.

5.2 Test Chip

The devices are fabricated on silicon wafers with 4mm x 4mm and 5mm x 5mm dimensions with approximate thicknesses of 400μm and 150μm respectively. The first set of devices has been fabricated in the Microfabrication Laboratory at Northeastern University as a part of the PhD project of Dr. Patricia Nieva [3]. The second series is fabricated using the PolyMUMPs fabrication process at MEMScAP laboratory [25].

5.2.1 Silicon Nitride Beam Process Flow

This process was developed in the Microfabrocation Laboratory at Northeastern University. It has one structural layer made of low stress silicon nitride and uses two masks which makes the process much simpler than the PolyMUMPs which requires eight masks. Unlike PolyMUMPs there is no electrical isolation layer deposited. More detailed information on this process in presented in Dr. P. Nieva PhD dissertation [3].

5.2.2 PolyMUMPs Process flow[3]

PolyMUMPs is a foundry process with three structural layers of polysilicon. This surface micromachining process is based upon the work performed at the Berkeley Sensors and Actuators Center (BSAC) at the University of California in the late 80's and early 90's. Since this is a general process, all structural layers have not been used in this work. In the following sections we first describe each step of the process and then will note whether it is used in the cantilever beams in this work.

---

[3] Information on PolyMUMPs process are partially based on PolyMUMPs Design Handbook.

Silicon wafer preparation

Devices are fabricated on a150 μm n-type <100> silicon wafers of 1-2 Ω-cm resistivity. The wafer surface is heavily doped with phosphorus in a standard diffusion furnace. This helps to reduce or prevent charge feedthrough to the substrate from electrostatic devices on the surface [25].

LPCVD deposition of Silicon Nitride (Electrical insulator)

A *600 nm* low-stress LPCVD (low pressure chemical vapor deposition) silicon nitride layer is deposited on the wafers as an electrical isolation layer [25]. This layer does not have any effect on the mechanical performance of the devices. But it changes the optical performance of the system and has to be considered in the optical calculations.

LPCVD deposition of Polysilicon (*Poly0*) and RIE etching

A *500 nm* LPCVD polysilicon film, *Poly0,* is deposited as the first structural layer. This layer can be patterned using *Poly0* mask. After patterning the photoresist, the Poly0 layer is then etched using plasma etching [25]. PolyMUMPs is a general process that can to fabricate different types of devices. As there was no application for this layer in this work, Poly0 layer is completely etched. Figure 5.3 shows the first three steps as described here.

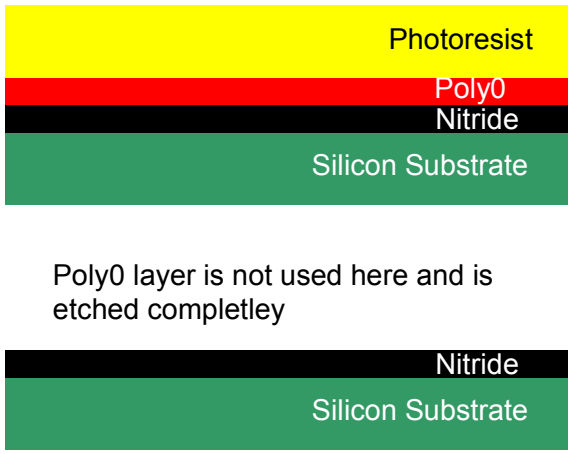

Figure 5.3 Poly0 layer deposition and RIE etching

Growing first oxide layer

A 2.0 μm phosphosilicate glass (PSG) sacrificial layer is then deposited by LPCVD and annealed at 1050°C for one hour in argon. This layer of PSG, known as First Oxide, will be removed at the end of the process to free the first mechanical layer of polysilicon.

Deposition of the first structural layer (Poly1) and RIE etching

After depositing and patterning the first oxide, the first structural layer of polysilicon (*Poly1*) is deposited at a thickness of *2.0 μm*. The wafer is then annealed at 1050°C for 1 hour. The annealing process significantly reduces the net stress in the *Poly1* layer. The polysilicon is lithographically patterned using the *Poly1* mask to form the first structural layer and it is etched using RIE. This layer is not used as a structural layer for the cantilever beams and is etched completely. Step four and five are shown in Figure 5.4.

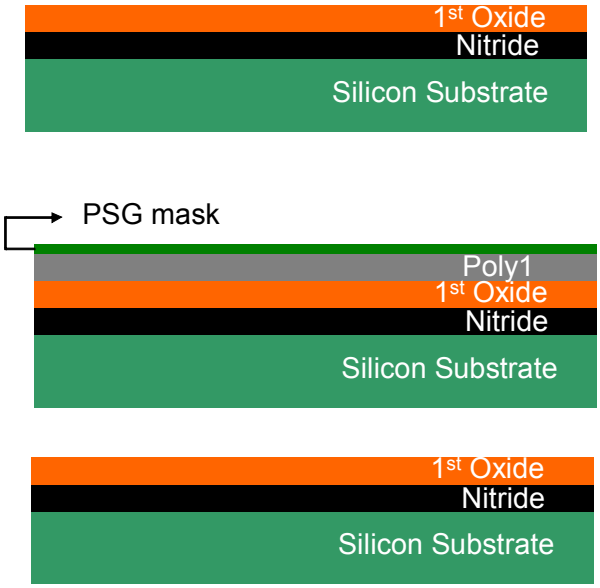

Figure 5.4 Depositing the first oxide layer and RIE etching

Growing second oxide layer and RIE etching

After etching the first structural layer, a second sacrificial PSG layer of 750nm is deposited and annealed. The Second Oxide can be patterned using two different etch masks. The *Anchor2* mask is used here to etch both the first and second oxide layers in one step.

Deposition of the second structural layer (Poly2) and RIE etching

After etching the second oxide layer, another structural layer of *1.5 μm*, *Poly2*, is deposited. It is followed by the deposition of *200 nm* PSG. The wafer is annealed for one hour at 1050 ^{o}C to dope the polysilicon and reduce the residual film stress. The *Poly2* layer is lithographically patterned with *Poly2* mask, and is etched by plasma and RIE processes. Figure 5.5 shows the above two steps.

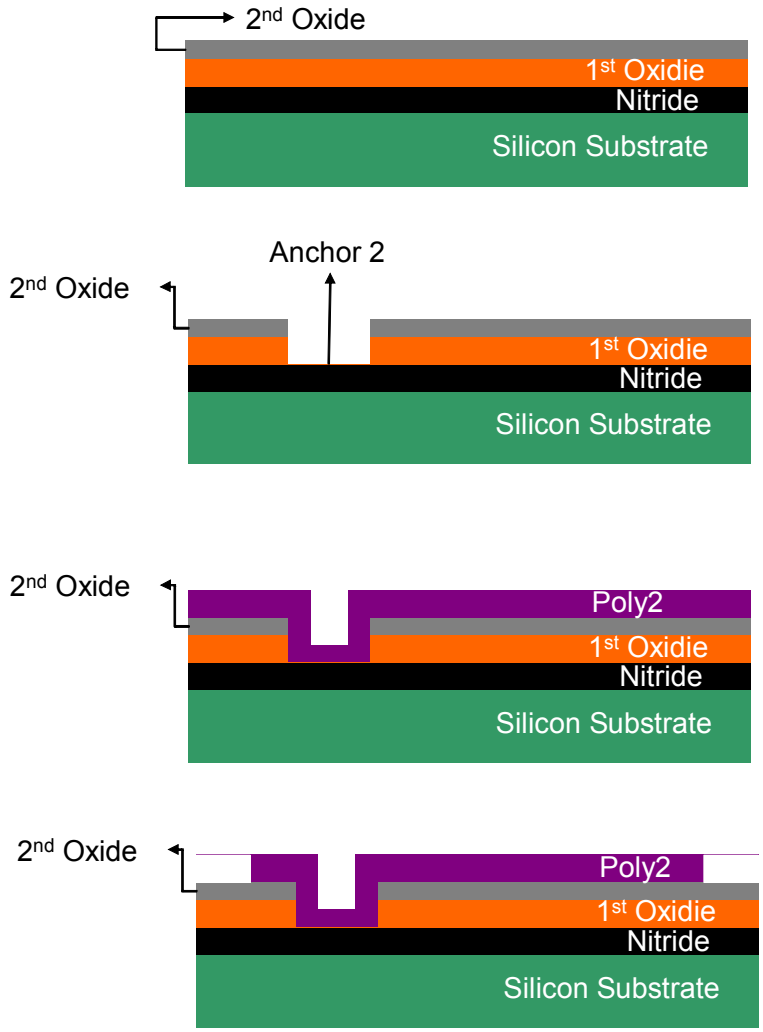

Figure 5.5 First structural layer deposition and RIE etching

Wet etch release and CO_2 drying

The chips are soaked in acetone for 20 minutes while agitated to remove the photoresist thoroughly. The chips are then placed in isopropyl alcohol for 10 minutes and then thoroughly rinsed in distilled water for 10 minutes. To release the structures are immersed in a bath of 49% HF at room temperature for 6 minutes to make sure that all devices are released. Then chips are rinsed fir 10 minutes in distilled water and soaked in isopropyl

alcohol three times each time for 8 minutes. The chips are then dried in a *Tousimis Automegasamdri-915B, Series C Critical Point* CO_2 dryer to avoid stiction.

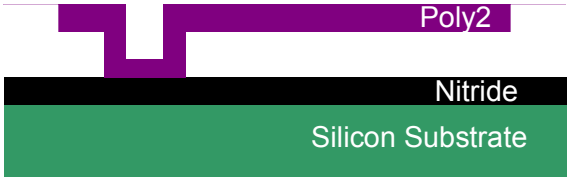

Figure 5.6 Releasing the sacrificial layer

Figure 5.7 shows the SEM pictures taken from the released devices. As it can be seen, the cantilever beams are completely released and free standing.

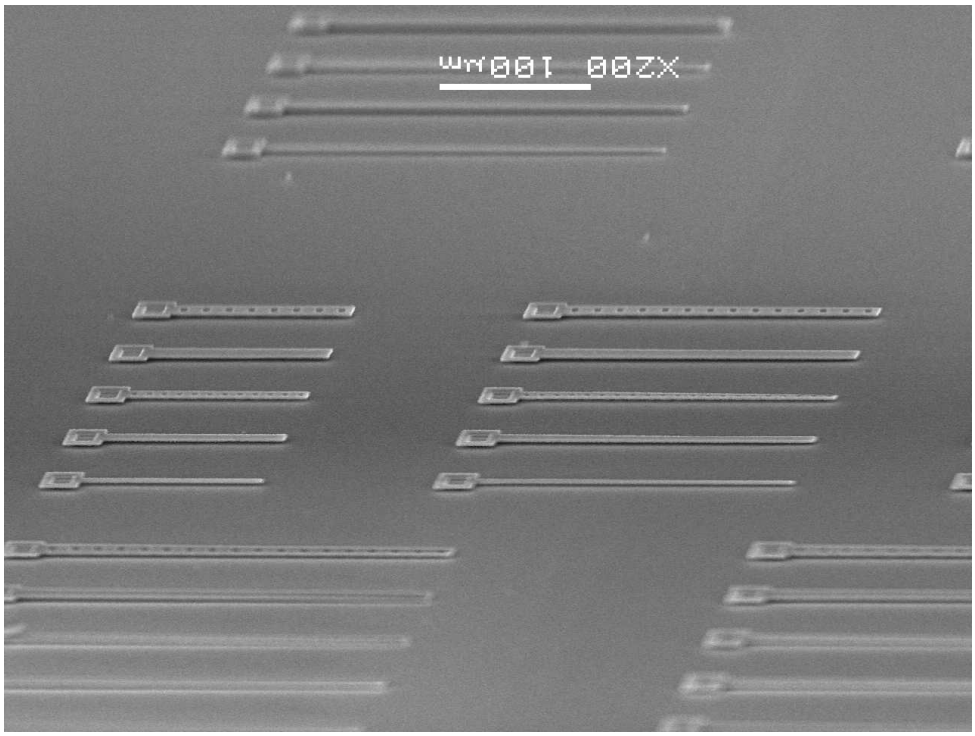

Figure 5.7 SEM Pictures of the released beams

A double-sided *Scotch* tape is used to bind the test chip to the piezoelectric actuator. Using this tape, the test chips can be easily removed from the actuator and replaced with another chip. Although, using tape makes it easy to replace the chips the pressure can squeeze the tape and the air bubbles between tape and the piezoelectric surface. Due to this problem, the system has to be focused each time that pressure is changed.

5.2.3 Piezoelectric Actuator

A ceramic based piezoelectric actuator manufactured by PI is used for excitation of the test chip. The piezoelectric actuator consists of a ceramic-encapsulated multilayer PZT (lead (*plumbum*)-zirconate-titanate) block, with solderable terminations as the electrical interface. The actuator is fixed on a custom-made pressure chamber (section 5.2.4) using nail polish for proper adhesion and insulation. Technical properties of the actuator are summarized in Table 5.1.

Table 5.1 Piezoelectric actuator technical properties

Model	PL-055.20
Material	Lead-Zirconate-Titanate
Number of layers (N)	50
Dimensions (A x B x thichness)	5 mm x 5 mm x 2 mm
Displacement	2.2 (μm @ 100V) ± 20%
Resonant frequency	>300 kHz
Operating Temperature Range	-20 °C to 85 °C
Electrical Capacitance	450 (nF) ± 20%

5.2.4 Pressure Chamber

To test the cantilever beams at different pressures, a pressure chamber was designed and fabricated. The main part of the pressure chamber is made out of aluminum. To allow for the laser beam to travel through the chamber the top lead is fabricated out of clear Plexiglass with *1cm* thickness. The plan view of the fabricated chamber is shown in figure 5.8. According to the manufacturer, to avoid crazing, the loads in Plexiglass should not exceed *1500 psi*. A FEM analysis was conducted to make sure that the chamber can withstand high pressures. The chamber is shown to be in the safe region for pressures up to *300 psi* , however, for safety issues the pressure is limited to *100 psi*. The chamber is connected to a pressurized pipe using a $1/4''$ *NPT* connector. The air pressure inside the chamber is controlled using a FESTO basic valve (LFR-D-5M-MIDI). The air is also filtered while passing through the valve with filtration grade of 5 μm . To avoid letting the air flow cause damage to the devices, the charging and discharging of the pressure is controlled with to valves. Figure 5.9 shows the pressure valve used in this work. To let the wires into the chamber, two brass screws are used and sealed using O-rings and thread sealant. The pressure chamber is located on an X-Y stage for micro-meter adjustment of the position of the test chip mounted on the piezo actuator with respect to the laser spot. The fabricated chamber is shown in figure 5.10.

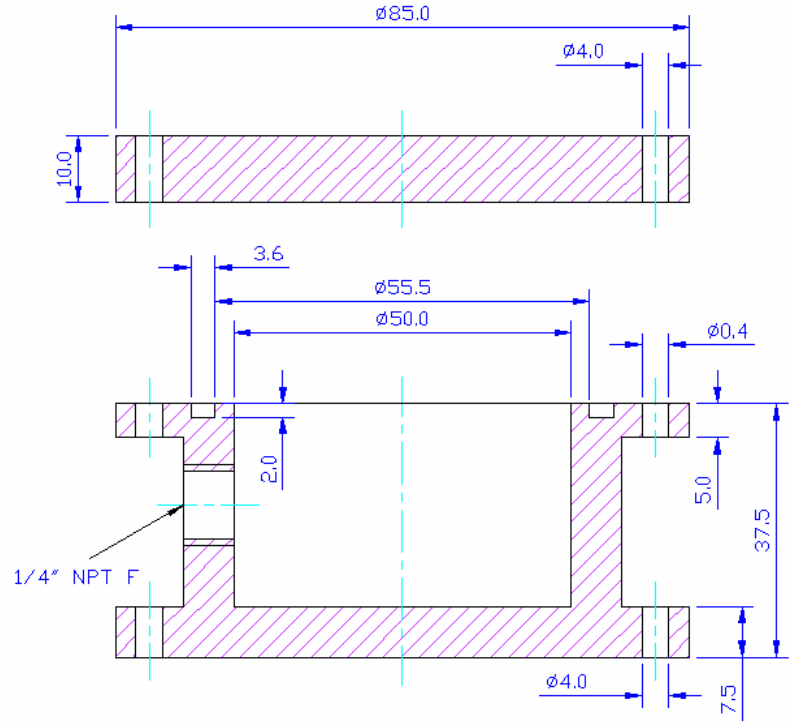

Figure 5.8 Pressure chamber drawings

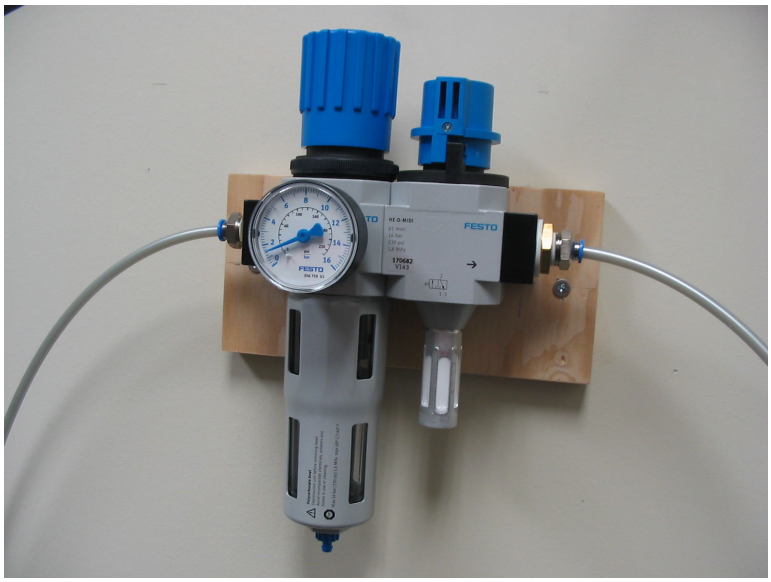

Figure 5.9 Pressure valve used to control the pressure inside the chamber

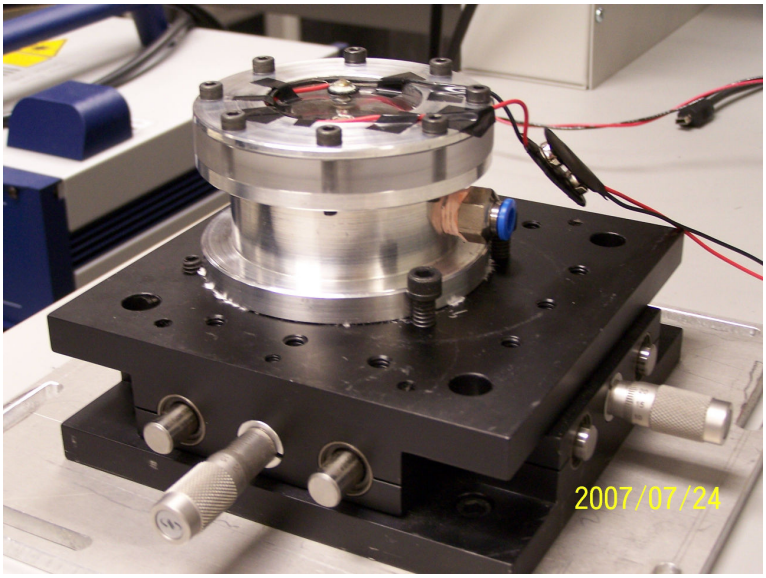

Figure 5.10 Pressure chamber place on an X-Y stage

5.2.5 Excitation Signal

The power consumption of a piezoelectric actuator is proportional to the frequency applied to it. As the applied frequency is increased, the power consumption of the actuator increases and therefore. It is crucial to use a power generation-amplification system that can supply the power needed for the frequencies of interest. The function generator that has been used for this work is a "20 MHz Function/Arbitrary Waveform Generator" (model number 33220A) manufactured by Agilent Technologies, Inc.[4] The sinusoidal signal generated by this function generator is amplified by an XP3000 Power Amplifier manufactured by Phonic Corporation.[5] LDV has been used for calibration of the mechanical excitation system by determining the displacement amplitude of the substrate. The principal of operation of the LDV is based on determination of velocity and displacement of the substrate from the Doppler shift of back-scattered laser light. The LDV used in this work is

[4] Agilent Technologies, Inc., Santa Clara, CA, USA

[5] Phonic Corporation, Tampa, FL, USA

manufactured by Polytec, Inc. and consists of an OFV-5000 Modular Vibrometer Controller and an OFV-551 Fiber-Optic Interferometer. More detailed information on the LDV can be found at www.polytec.com. Displacement measurement is explained in detail in [3].

5.2.6 Calibration of the Mechanical Excitation System

To find the frequency response of the system, the mechanical excitation system has to be calibrated. The calibration is performed to find the input voltage at different frequencies which generates the same amount of displacement. In this work, the substrate displacement is tried to be close to 10nm for all applied frequencies. To find the input voltage that results in 10 nm displacement, the LDV system is used here. First the controller peak to peak voltage that corresponds to 10 nm movement has to be found. After finding the peak to peak voltage values for different frequencies, the piezoelectric shaker is excited by applying a frequency and an input voltage. The velocity signal from the LDV is then recorded from the oscilloscope. To reduce the noise effect, the oscilloscope is set to average the signal for 8 (or 16) times. The velocity signal is then compared with the desired input signal. If the displacement value is not within the acceptable range ($\pm 2\%$) the input signal has to be adjusted to approach the desired value.

The calibration process needs to be completed for all the frequencies in the working range. At the end of the sequence, the calibration process is performed once again using the recorded values to check the results obtained in the first round.

5.3 Electro-Optical Measurement System

The electro-optical measurement system is shown in Figure 5.11. The working principle of the system is based on the measurement of the total reflected signal from the device. The system theory is described in chapter 3.

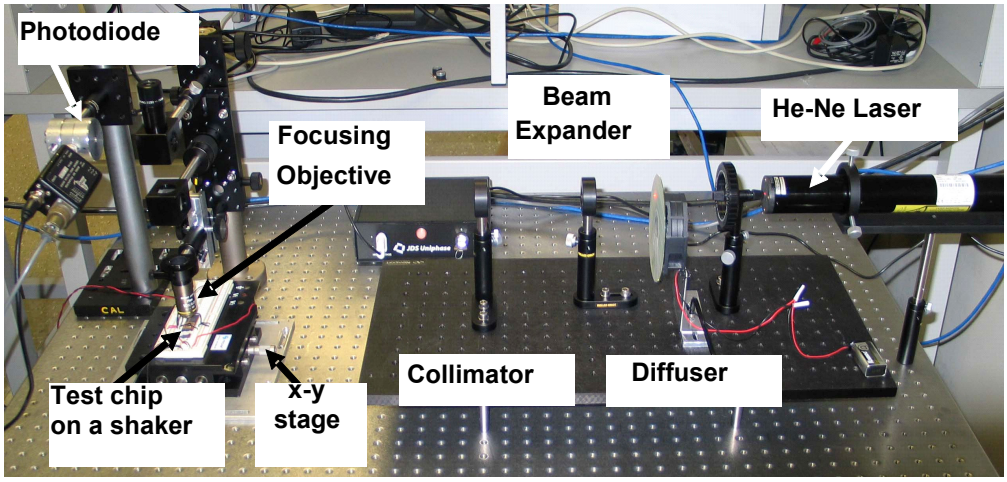

Figure 5.11 Electro-Optical measurement system

The electro-optical measurement system is a non-contacting measurement system, and can have very high positional resolution. As mentioned before, the system detects the displacement by measuring the amplitude of the back-reflected interferometric signal of the vibrating beam. A reflected light is obtained by directing the light beam of a He-Ne laser (wavelength $\lambda = 632.8\,\text{nm}$) focused to a 15μm spot at normal incidence to a specific location on the surface of the beam. The power reflectance of the reflected light is measured by a photodiode and is then amplified using a trans-impedance amplifier. The measure optical signal is then recorded using a DSO3000 Agilent oscilloscope. The recorded signals are then processed by a Matlab code and the frequency response of the system is determined.

Although the system is only used for the displacement measurement, it is also equipped with an eyepiece lens. The eyepiece lens and the objective lens create a microscope that can be used to see the spot position on the device. In order to focus a laser beam with a diameter of 0.80mm to a spot size of 15μm to 20μm, multiple lenses are used. A plano-concave lens near the source of the laser expands the 0.80mm diameter beam over a distance of 129mm to a 16mm diameter. At this distance, an achromat lens is positioned to collimate the beam as it is headed towards a beam-splitter. The beam expansion is necessary to get a small spot. The beam-splitter redirects approximately 50% of the beam downwards onto a 10X microscope objective lens. The laser is being focused at the focal distance from the bottom of the objective lens. The cantilever beam has to be placed at the focal frontal focal point of the objective for the laser beam to be focused on that with a 15μm spot. Finally, the back reflection coming from the device is directed equally to the eyepiece for inspection and the photodiode to obtain the reflected signal using a mirrored beam splitter.

5.3.1 Calibration of the Electro-Optical Measurement System

To extract the optical parameters which are required to find the displacement of the beam, the optical system has to be calibrated. As mentioned in chapter 3, displacements larger than $\lambda/4$ result in a nonlinear optical signal which can be uniquely fitted to the optical model result. Using this nonlinearity specification, this signal can be used for parameter extraction. To generate this signal, a large relative motion is required. This motion can be obtained at any frequency and highly depends on the piezoelectric limitations. To be able to get this signal it is better to start with frequencies at which the shaker generates larger displacement and the input voltage has to be increased to get the signal. It is also possible to find this signal

at frequencies close to the natural frequency of the device. Once the signal is obtained it is recorded using the USB interface. The signal is processed using a Matlab code and it is fitted to the optical model developed in chapter 3. The parameters that are obtained from the fitting process (cantilever thickness, initial gap and etc) are used in the rest of the analysis to process the optical signals at different frequencies.

5.4 Experimental Frequency Response and Pressure Measurement

After the calibrating the mechanical and the electro-optical systems, the experimental frequency response can be determined by exciting the device using the frequency and voltage settings recorded during the calibration of the mechanical excitation system. This way the chip is excited with a constant known frequency over the measurement range. The electro-optical system measures the optical power coming from the photo detector and a signal recorded for each frequency. To obtain an accurate measurement the effect of this electromagnetic coupling has to be deducted from the optical signal. The electromagnetic coupling signal has to be recorded at each frequency with the same setting that is used to record the optical signal. To obtain this signal, the laser light has to be blocked. Once these signals are recorded for the frequencies of interest, a Matlab code (Appendix 2) is used to perform the analysis and calculate the relative motion of the beam with respect to the substrate. This process is repeated at different pressure conditions and the frequency responses of the cantilever beam are recorded. The experimental frequency responses are then fitted to the theoretical model presented in Chapter 3 using pressure as a fitting parameter.

Chapter 6
Results and Conclusions

In this chapter the experimental frequency response of two sets of cantilever beams are presented. Each beam is tested for a range of 5 to 140 kHz at different pressures. The test procedure and the system calibration method were described in Chapter 5.

Each cantilever beam has been tested at different pressures and the frequency response of the device under each pressure condition is derived. The frequency responses obtained, are fitted to the theoretical model developed in Chapter 2. Air pressure is used as the fitting parameter. The fitted pressure and the actual pressure are compared. The fitted data is used to sense the pressure. The sensor minimum detectable pressure is then analyzed and presented in the rest of this chapter.

6.1 Mechanical Analysis

The experimental frequency response is obtained by exciting the substrate of the cantilever beam at a constant nanometer displacement and recording the optical interferometric signal. The optical signal is recorded at different frequencies of the range within interest (5 to 140 kHz). The recorded optical signals are then processed using the fitting parameters found from the optical calibration and the relative displacement of the cantilever beam with respect to the substrate is calculated. The relative displacements are then divided by the substrate movement to find the frequency response. The experimental results are then fitted to the mechanical theory developed in chapter 2. They are also compared with the results obtained from the theoretical model.

6.1.1 Experimental Frequency Response

The measured dimensions of the tested cantilever beams are presented in table (6.1) and (6.2). These values are used to compare the model results with the experimental results.

Table 6.1Silicon nitride beam dimensions

Silicon Nitride Beam	
Spot Location	17.5 μm
Length	89.22 μm
Width	9.31 μm
Thickness	0.44 μm
Gap height at anchor	1.4121 μm
Epsilon	0.02
Number of holes	10
Hole width	3.43 μm

Table 6.2 Silicon nitride beam dimensions

PolyMUMPs Beam	
Spot Location	5 μm
Length	263 μm
Width	9.3 μm
Thickness	1.42 μm
Gap height at anchor	1.64 μm
Epsilon	-0.14

The nitride beam was tested at *1 atm (14.69 psi)*, *40 psi*, *60 psi* and *80 psi*. Each test condition is repeated for three times and average values of them were plotted. Figure (6.1) shows the results obtained for these beams for the tested pressures.

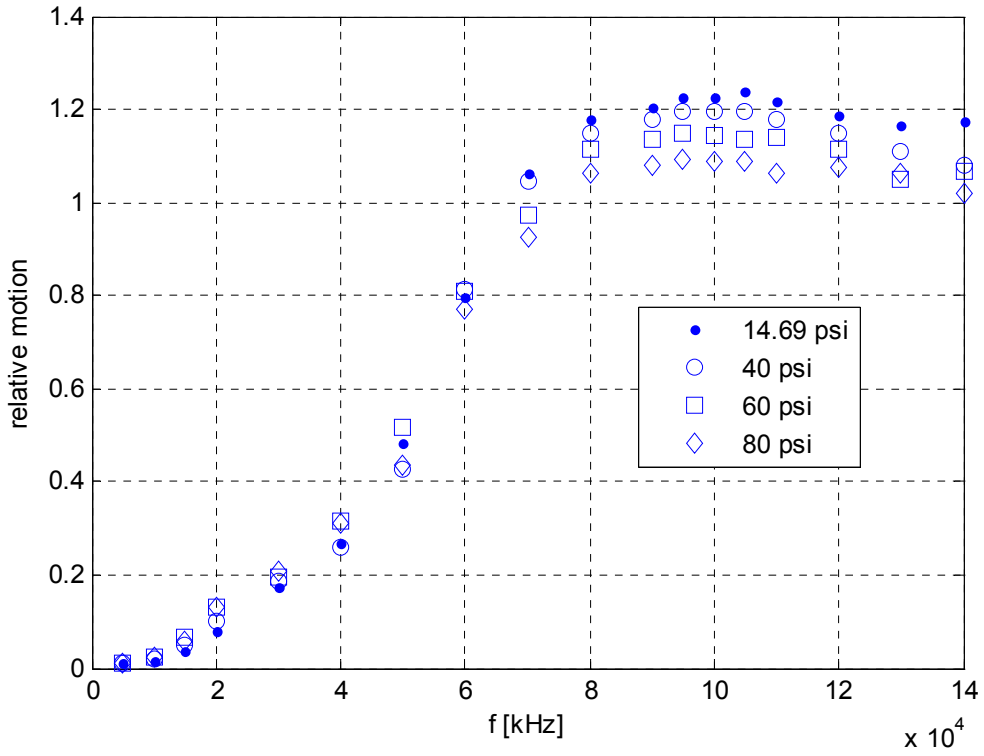

Figure 6.1Frequency response of the silicon nitride beam at different pressures

As it was expected, the graph shows that the relative motion decreases at frequencies close to the natural frequency with pressure increasing. As it is shown in chapter 2 the squeeze film damping does not change with pressure, however increasing the pressure (density of air) increases the airflow damping which affects the relative motion at frequencies close to the

natural frequency of the beam. The PolyMUMPs device is also tested at 1atm, 40psi and 90psi. The frequency response for the polyMUMPs beam is shown in Figure (6.2).

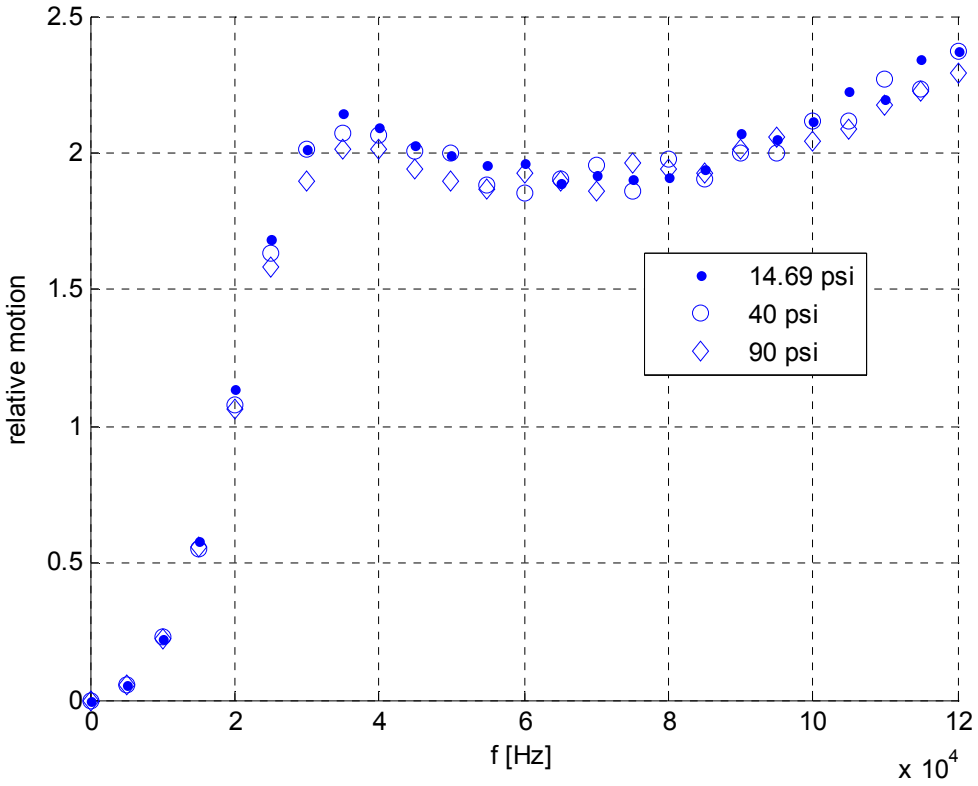

Figure 6.2 Frequency response of the PolyMUMPs beam at different pressures

6.1.2 Frequency Response: Experimental versus Fitted

The experimental frequency responses presented in the previous section were fitted to the mechanical theory developed in chapter 2. The average temperature of the lab was $25^{o}C$. Since, the piezo acts as a heat source while it is operating; the temperature in the enclosed chamber is higher than the lab's temperature. The working temperature is considered to be

$30^{o}C$ to account for the piezo heat generation. The frequency response equations are presented in this section for convenience. The off-diagonal terms are neglected for the fitting purpose.

$$\delta_R = \sum\left(A_i \frac{h_0}{Z_0}\Phi_i \right) \tag{6.1}$$

$$\begin{Bmatrix} A_1 \\ \vdots \\ A_n \end{Bmatrix} = \begin{bmatrix} \dfrac{1}{1+2\zeta_1\left(\dfrac{\omega}{\omega_1}\right)-\left(\dfrac{\omega}{\omega_1}\right)^2} & & \\ & \ddots & \\ & & \dfrac{1}{1+2\zeta_n\left(\dfrac{\omega}{\omega_n}\right)-\left(\dfrac{\omega}{\omega_n}\right)^2} \end{bmatrix} \times \begin{Bmatrix} \dfrac{Z_0}{h_0}\left(\left(\dfrac{\omega}{\omega_1}\right)^2 - i\dfrac{1}{\rho A_{eff}}\dfrac{\omega}{\omega_1^{\,2}}\right)\displaystyle\int_0^1 \Phi_1 dX \\ \\ \dfrac{Z_0}{h_0}\left(\left(\dfrac{\omega}{\omega_n}\right)^2 - i\dfrac{1}{\rho A_{eff}}\dfrac{\omega}{\omega_n^{\,2}}\right)\displaystyle\int_0^1 \Phi_n dX \end{Bmatrix} \tag{6.2}$$

The first two modes of the system are used for the fitting process. As it can be seen from Equation (6.2), this model depends on the damping factors and the structural fundamental frequencies of the cantilever beam. The structural fundamental frequencies of the beam can be calculated using the Young's modulus and cantilever beam dimensions as follows:

$$\omega_n = \beta_n^{\,2}\sqrt{\frac{EI_y}{\rho w d L^4}} \tag{6.3}$$

The damping factor for each mode is as follows:

$$\zeta_i = \frac{1}{2\alpha_i^{\,4}}\left[C_2 C_a \frac{\omega h_0}{p_a b} - C_2 \int_0^1 \Phi_i imag\left(F_{squeeze}\big|_i\right) dX \right]\left(\frac{\omega_n}{\omega}\right) \tag{6.4}$$

Where $C_2 = \frac{p_a b l^4}{EIh_0}$ and C_a is the airflow damping coefficient.

The damping factor can be written as the sum of airflow and squeeze film damping factor

$$\zeta_i = \zeta_{airflow} + \zeta_{squeeze} \tag{6.5}$$

The squeeze film damping does not depend on the ambient pressure. Also, calculating the squeeze film damping at different squeeze number values shows that the squeeze film damping factor is constant over the frequency range of interest. Hence, the squeeze film damping can be calculated independent of pressure values. On the other hand the airflow damping coefficient is a function of pressure and frequency. By calculating the airflow damping coefficient at the beam's fundamental structural frequencies, the airflow damping damping factor will be function of ambient pressure only. Utilizing the MATLAB optimization tools, the pressure can be found in such a way to minimize the root mean square of the error. Error is defined as the difference between the experimental results and model output. The MATLAB code that is used in this work is presented in Appendix B. The fitted frequency responses and the theoretical results at each pressure for both sets of devices are shown in Figures (6.3) to (6.9).

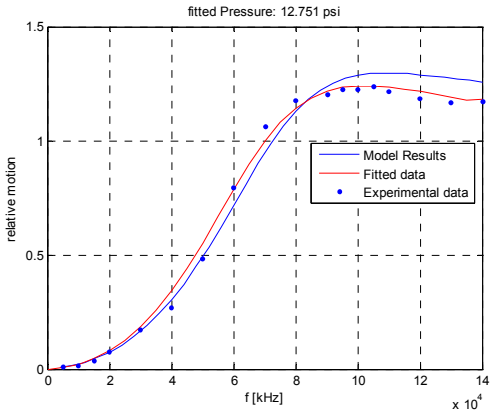

Figure 6.3 Comparison of the fitted, measured and calculated frequency response at *1* atm

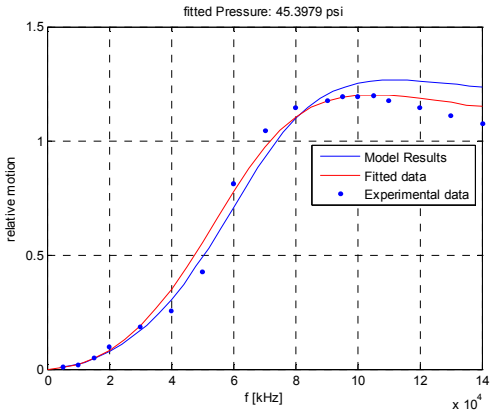

Figure 6.4Comparison of the fitted, measured and calculated frequency response at *40* psi

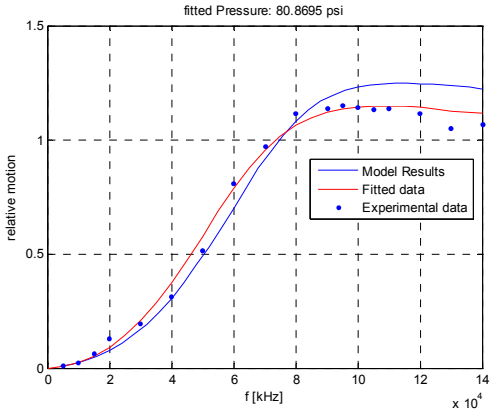

Figure 6.5 Comparison of the fitted, measured and calculated frequency response at *60* psi

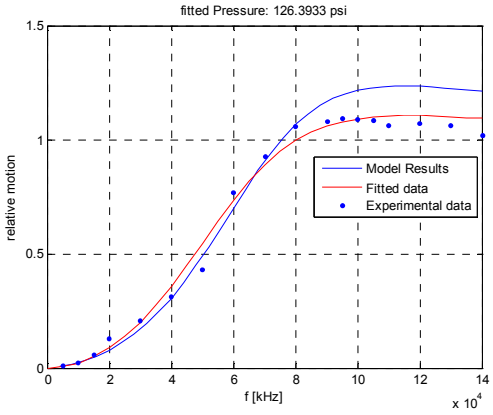

Figure 6.6 Comparison of the fitted, measured and calculated frequency response at *80* psi

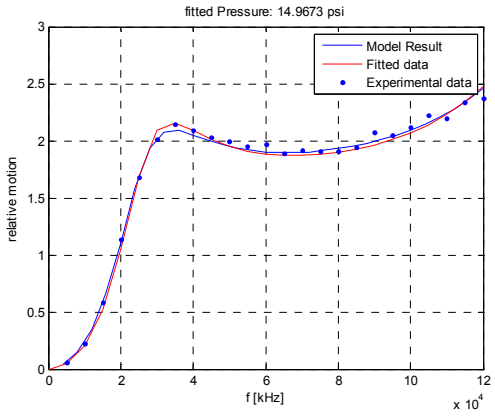

Figure 6.7Comparison of the fitted, measured and calculated frequency response at *1atm*

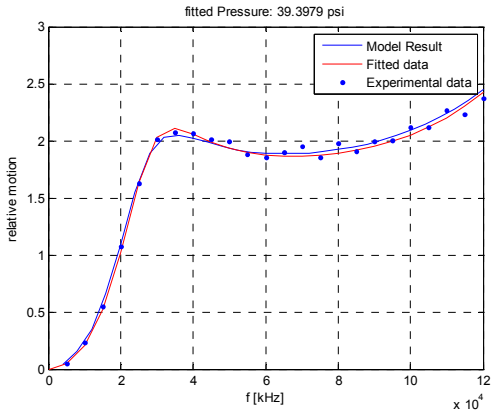

Figure 6.8 Comparison of the fitted, measured and calculated frequency response at *40* psi

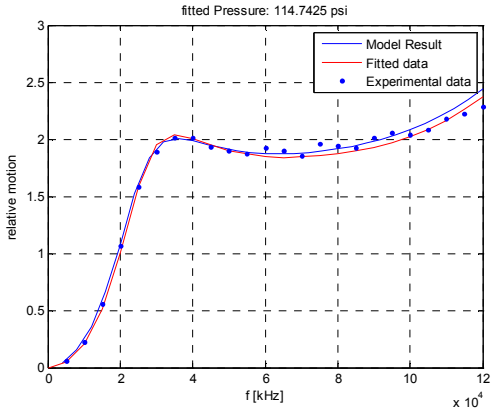

Figure 6.9 Comparison of the fitted and measured frequency response at *90* psi

The applied pressure at the gauge and the estimated pressure are presented in table 6.3 and 6.4 for silicon nitride and PolyMUMPs beams. As it can be seen from the results, both sensors, especially the PolyMUMPs fabricated sensor, predict the low pressures with good accuracy. However, the error grows as pressure increases.

Table 6.3Applied pressure and estimated pressure for silicon nitride sensor

	Silicon Nitride			
Pressure at the gauge (psi)	14.69	40	60	80
Fitted pressure (psi)	12.75	45.39	80.86	126.39
Error $(\frac{P_{applied} - P_{fitted}}{P_{applied}} \times 100)$	15.21	11.89	25.81	36.71

Table 6.4 Applied pressure and estimated pressure for PloyMUMPs sensor

	PolyMUMPs		
Pressure at the gauge	14.69	40	90
Fitted pressure	14.96	39.397	114.49
Error $(\frac{P_{applied} - P_{fitted}}{P_{applied}} \times 100)$	1.84	1.51	27.49

This problem can be related to the fact that the relative displacement is less sensitive to the pressure at higher pressures and causes the error to increase. Figure 6.10 shows the displacement sensitivity to the pressure for different pressure values for the PolyMUMPs sensor. This calculation is conducted at the fundamnetal frequency of the beam. As it is shown in the figure the sensitivity decreases at high pressures

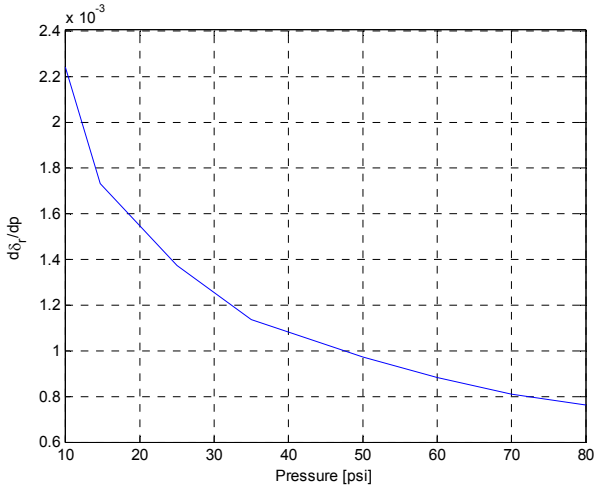

Figure 6.10 Displacement sensitivity to pressure plotted against the pressure

Another way to compare the model and the experimental results is to monitor the shift in the natural frequency of the system. The applied pressure can also be estimated using the shifting value. The natural frequencies at different pressure are compared for model and experimental data in the following tables 6.5 and 6.6. Note that the natural frequency shift ratio is calculated based on the difference between the two adjacent entries.

Table 6.5 Applied pressure and the natural frequency for the Nitride device

	Model Calculations		Experimental Results	
Pressure (psi)	Natural frequency (Hz)	$\Delta f / \Delta p_a \left(\frac{Hz}{psi}\right)$	Natural frequency (Hz)	$\Delta f / \Delta p_a \left(\frac{Hz}{psi}\right)$
14.69	109110	101.54	102700	106.67
40	111680	74	105400	130
60	113160	73.5	108000	100
80	114630		110000	

Table 6.6 Applied pressure and the natural frequency of the PolyMUMPs device

	Model Calculations		Experimental Results	
Pressure (psi)	Natural frequency (Hz)	$\Delta f / \Delta p_a \left(\frac{Hz}{psi}\right)$	Natural frequency (Hz)	$\Delta f / \Delta p_a \left(\frac{Hz}{psi}\right)$
14.69	35526	24.94	33800	19.755
40	36158	20.91	34300	16.00
90	37105		35100	

As we can see for the PolyMUMPs device the frequency shifting to the pressure ratio is lower from the model results by the value of 5 *Hz/psi*. However, for the nitride device, the offset value is not constant and is varying with pressure. Using the theoretical model it can be shown that the frequency shifting to the pressure is decreasing for low pressures and then becomes steady. This shows that the ambient pressure can be linearly estimated as a function of natural frequency of system.

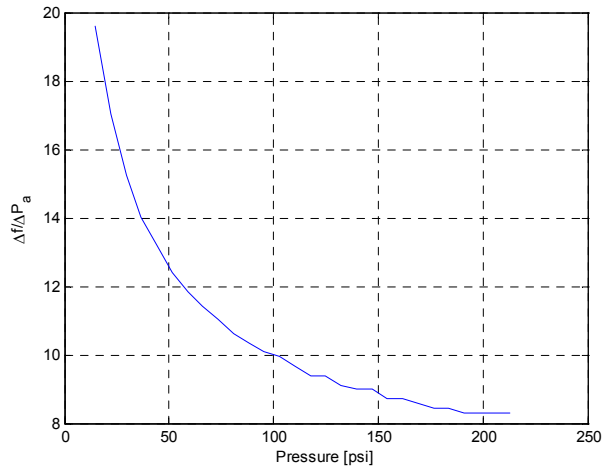

Figure 6.11 The ratio of natural frequency shifting to ambient pressure versus pressure

6.2 Minimum Detectable Pressure difference

One of the most important parameters for each sensor is the minimum detectable value at each working condition. This analysis can be used to indicate the regions that the sensor can be used with the best resolution. This section is devoted to the minimum detectable pressure difference for the proposed sensor. The analysis is limited to the case of PolysMUMPs fabricated sensor.

The minimum detectable pressure difference in the presented sensor is based on the noise level in motion detection circuits and the noise generated by thermal disturbances. In the proposed sensor, the pressure measurement is calculated based on the relative motion of the cantilever beam. Hence, to be able to find the minimum detectable pressure difference, first the minimum detectable displacement has to be calculated. The minimum detectable pressure difference can then be calculated using the following Equation:

$$\Delta P = \frac{\partial P}{\partial \delta_r} \Delta \delta_r \tag{6.6}$$

By calculating the maximum level of the noise in the system the minimum measurable displacement can be obtained by setting the level of the signal to noise ratio (SNR) to unity [3]. In other words, if SNR becomes slightly greater than unity the signal is considered to carry reliable reading. The signal to noise ratio is defined as

$$SNR = \frac{\left\langle \delta_r{}^2 \right\rangle}{\left\langle \delta_d{}^2 \right\rangle + \left\langle \delta_{th}{}^2 \right\rangle} \tag{6.7}$$

Where, δ_r is the detected displacement signal, δ_d is an equivalent mechanical displacement corresponding to the electrical noise in the system, and δ_{th} is the thermal mechanical noise existing in the system.

The major components of the electrical noise in the system are laser noise (i_L), Johnson noise due to the shunt resistor ($i_{R_{SH}}$), shot noise (i_{sh}), and the Johnson noise due to the feedback resistor in amplifier (i_{R_F}) [3].

The laser light source used for the experiments has maximum noise of 0.2% (rms) in the frequency range of 30HZ to 10MHZ which leads to laser noise of $i_L = 4.1\times10^{-12}\,\text{A(rms)}/\sqrt{\text{HZ}}$. The photodiode shunt resistor for the specific photodiode used is $R_{SH} = 0.5\text{M}\Omega$, and the resulting noise current is $i_{RSH} = 1.8\times10^{-13}\,\text{A(rms)}/\sqrt{\text{HZ}}$. Shot noise is generated by random fluctuations in PN junction of the photodiode and is a function of the total DC current through the diode ($i_{DC} = 7.35\times10^{-7}\,\text{A}$). Consequently the shot noise is $i_{sh} = 4.85\times10^{-13}\,\text{A(rms)}/\sqrt{\text{HZ}}$. Finally the noise due to the feedback resistor is calculated $i_{RF} = 1.28\times10^{-12}\,\text{A(rms)}/\sqrt{\text{HZ}}$. Using the mechanical displacement to electrical current sensitivity ratio and the summation of rms values of all noise currents, equivalent mechanical displacement corresponding to the electrical noise in the system (δ_d) is calculated $\delta_d = 3.93\times10^{-14}\,\text{m}/\sqrt{\text{HZ}}$. The more detailed information on the above mentioned noise sources and calculation methods are presented in [3].

The thermal mechanical noise is mainly due to molecular agitation of the beam by surrounding air particles or thermal-statistical fluctuations of the structure. The rms of the displacement at the free end of a cantilever beam can be approximated using the following Equation [3]

$$\left\langle \delta_{th}{}^{2}(L) \right\rangle \approx \sum_{n=1}^{N} \frac{2k_B T c_n \phi_n{}^{2}(L)\Delta f}{m_n{}^{2}\omega_n{}^{4}} \tag{6.8}$$

where, k_B is the Bultzmann's constant, T is the ambient temperature, c_n is viscous damping coefficient for the nth mode of vibration, ϕ_n is the modal shape for the nth mode of vibration, m_n is the modal mass and ω_n is the modal frequency. The thermal-mechanical noise calculated for the beam under experiment is calculated to be $\delta_{th} = 1.23 \times 10^{-14}\,\mathrm{m}/\sqrt{\mathrm{HZ}}$. Considering Equation (6.7) and setting the SNR to unity, the equivalent displacement of the beam caused by noises is calculated which can also be called the minimum detectable displacement $\delta_r = 4.14 \times 10^{-14}\,\mathrm{m}/\sqrt{\mathrm{HZ}}$. Finally, the minimum detectable pressure differences for the mentioned sensor are calculated using Equation (6.6). The values regarding the pressure sensitivity to the displacement can be found from Figure (6.10). Table 6.5 summarizes the results at 1atm (14.7 psi) and 30 ^{o}C.

Table 6.7 Sensitivity of the sensor in different ambient pressures

P (psi)	Minimum Detectable Pressure Difference ($psi/\sqrt{Hz}$)
14.69	0.75

6.3 Conclusions

As it can be seen from tables 6.3 and 6.4 at low pressures, the predicted pressure and the applied pressure are close to each other. However, the error increases with the pressure as the pressure increases. This can be justified with the fact the pressure sensitivity of the sensors decreases with pressure (as shown in figure 6.10) which causes pressure differences even for very small deviation from the model predicted results. Another possible source of error can be the thermal-mechanical noise. In the analysis presented in the previous section the thermal-analysis noise was considered at the atmospheric pressure. The effect of pressure on this parameter has to be investigated in future work.

The natural frequency shifting with pressure is presented in this section shows that the natural frequency becomes a linear function of pressure, which makes it a very good parameter for the pressure measurements.

The predicted pressure values are off for both sensors at high pressures, as shown in tables 6.3 and 6.4 this problem is more obvious for the silicon nitride beam. For the PolyMUMPs fabricated beam the theoretical results and the experimental results are in a very good agreement and the deviation is only observable at frequencies close to the second natural frequency of the system. This can be due to the fact the model is evaluated using only the

first to modes of vibration. However, the model results for the nitride beam stand above the experimental frequency response. The experimental results and the model results are in good agreement at low frequencies were the damping is not an important factor, but the difference increase at frequencies closer to the natural frequency of the beam. In Chapter 3 the holes are assumed to be frictionless and they only work as a vent that let the air escape freely. This assumption can be considered as the main reason for the difference shown in nitride beam results which causes a great error in the estimated pressure.

6.4 Future Work

As shown in this chapter, the proposed sensor is more sensitive at lower pressures. In this work, the sensor is only tested at high pressures. While measurement errors increase with pressure, calculations show that the sensor is more sensitive for low pressure measurements. Therefore, it is suggested to equip the fabricated pressure chamber with a vacuum pump and conduct a series of measurements at lower pressures.

The thermal-mechanical noise in this work is investigated at the atmospheric pressure, the effect of pressure on this factor can be one of the reasons that the sensor resolution decreases with pressure. This parameter has to be evaluated at high pressure in future work.

As mentioned before the squeeze film damping is the dominant damping term and governs the results at frequencies close to the natural frequency of the system. As shown in Chapter 3 the squeeze film damping is not a function of pressure. In order to increase the pressure sensitivity of the system, sensors with larger gap height have to be fabricated and tested to see the effect of gap height on the predicted pressure.

The squeeze film damping is highly dependent on the viscosity of the air. Viscosity also varies with the air temperature. Therefore, this sensor with the current configuration can be investigated at different temperatures for possible utilization as a temperature sensor.

The conducted tests were assumed to be at $30^{o}C$, it is suggested to control the air temperature in the chamber for the future tests.

Appendix A
Multi Layer Beam Theory

Multilayer films are widely used in science and industry for control of light. Using this theory, optical surfaces with any desired reflectance and transmittance can be built [26]. To develop the multilayer film theory, we first consider the case of a single layer of dielectric with index of refraction n_1 and thickness t_1 between two infinite media with indices n_0 and n_t (shown in figure 3.1). Since the beam deflection is very small, as was discussed in chapter 2, we assume the light to be normal to the surface. The boundary conditions require that the electric and magnetic fields be continuous at each interface [26]. These conditions are expressed as follows:

At first interface:

Electric: $$E_0 + E_0' = E_1 + E_1' \tag{A.9}$$

Magnetic: $$H_0 - H_0' = H_1 - H_1' \tag{A.10}$$

At second interface:

Electric: $$E_1 e^{ikl} + E_0' e^{-ikl} = E_T \tag{A.11}$$

Magnetic: $$H_1 e^{ikl} - H_0' e^{-ikl} = H_T \tag{A.12}$$

Where, E_0, E_0' are amplitude of the electric vector of the incident and the reflected beam for the first interface respectively. The electric-field amplitudes in the film are E_1, E_1' for the

forward and backward traveling waves respectively. The transmitted electric field amplitude is E_T, as indicated in figure 3.1. The same terminology is used for magnetic field amplitude. The phase factors e^{ikl}, e^{-ikl} are due to the fact that the wave travels through a distance l from one interface to the other.

For plane waves the relation between H and E is as follows [26]:

$$H = \frac{nE}{Z_0} \tag{A.13}$$

in which Z_0 is known as the *impedance of free space*.

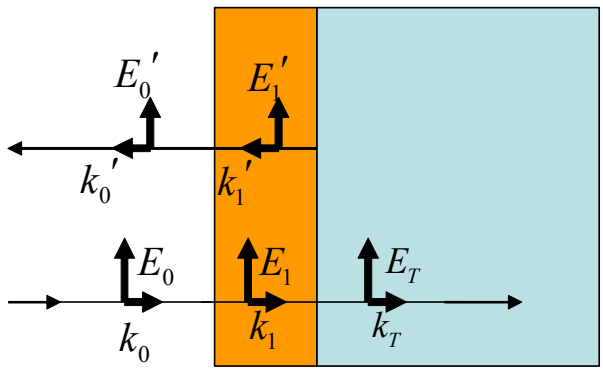

Figure A.1 Wave vector and their electric field for the case of normal incidence on a single dielectric layer

Substituting equation(A.13) in equations(A.10) and (A.12) and rearranging the equations in matrix form we have:

$$\begin{bmatrix} 1 \\ n_0 \end{bmatrix} + \begin{bmatrix} 1 \\ -n_0 \end{bmatrix} r = M \begin{bmatrix} 1 \\ n_T \end{bmatrix} t \tag{A.14}$$

where, $r = \frac{E_0'}{E_0}$, $t = \frac{E_T}{E_0}$ are reflection and transmission coefficients respectively.

The matrix *M*, known as the transfer matrix, has the following form:

$$M = \begin{bmatrix} \cos kl & \frac{-i}{n_1}\sin kl \\ -in_1 \sin kl & \cos kl \end{bmatrix} \tag{A.15}$$

where n_1 is the complex index of refraction and $k = \frac{2\pi}{\lambda} n_1$.

The above theory can be expanded for the case of more than one layer and it can be shown that the reflection and transmission coefficients of the multilayer film are related by a similar matrix equation.

$$\begin{bmatrix} 1 \\ n_0 \end{bmatrix} + \begin{bmatrix} 1 \\ -n_0 \end{bmatrix} r = \underbrace{M_1 M_1 \cdots M_N}_{M} \begin{bmatrix} 1 \\ n_T \end{bmatrix} t \tag{A.16}$$

where $M_1, M_2 \cdots M_N$ are transfer matrices of different layers. The overall transfer matrix *M* is the product of the individual transfer matrices. Equation (A.16) can be solved for reflection and transmission coefficients:

$$r = \frac{An_0 + Bn_T n_0 - C - Dn_T}{An_0 + Bn_T n_0 + C + Dn_T} \tag{A.17}$$

$$t = \frac{2n_0}{An_0 + Bn_T n_0 + C + Dn_T} \tag{A.18}$$

where A, B, C and D are the elements of the overall transfer matrix. Knowing r and t reflectance R and transmittance T can be calculated as follows:

$$R = \left|r^2\right| = rr^*, \qquad \mathrm{T} = \left|t^2\right| = tt^* \tag{A.19}$$

in which the asterisk denotes the complex conjugate.

Appendix B

MATLAB Codes

Mechanical Frequency Response Calculator

```
clc
clear

%%%%%%%%%%%%%%%%%%%%%%% Input Data %%%%%%%%%%%%%%%%%%%%%%

    %%%%%%%%%%%%%%%%%%% Young Modulus & Density %%%%%%%%%
    E = 158e9;
    rho_Poly = 2330;

    %%%%%%%%%%%%%%%%%%% Cantilever Beam Dimensions %%%%%%
    L_beam = 263e-6;
    W_beam = 10e-6;
    t_beam = 1.42e-6;
    h0 = 2.75e-6;  %% Air gap at the anchor
    epsilon = -0.14;  %% Beam curvature
    Iy = W_beam*t_beam^3/12;

    %%%%%%%%%%%%%%%%%%% Spot Location %%%%%%%%%%%%%%%%%%%
    spot = 5e-6;  %% From the tip
    spot_ratio = (L_beam-spot)/L_beam;

    %%%%%%%%%%%%%%%%%%% Air Properties %%%%%%%%%%%%%%%%%%%
    Pa = 1*1e5;
    mu = 1.8e-5;
    rho_air=(Pa/1e5)*1.3;

    Z0 = 10e-9;
    No_Mode = 2;


%%%%%%%%%%%%%%  Structural Mode Shapes   %%%%%%%%%%%%%%
syms x
for  Mode_No = 1:No_Mode
    cant = [1.8762 4.6904 7.8549];  % beta_n*l refer to "Theory of
Vibration with application" pp. 273
    ALPHA = cant.^4;
    bb = cant(Mode_No);
    Mode(Mode_No) = (cosh(bb*x) - cos(bb*x)) - ((cosh(bb) +
cos(bb))/(sinh(bb) + sin(bb)))*(sinh(bb*x) - sin(bb*x));
    W2 = eval(int(Mode(Mode_No)*Mode(Mode_No),x,0,1));  % Mode shape
amplitude used to normalize the structural mode shapes
    Normalized_W(Mode_No) = Mode(Mode_No)/sqrt(W2);
```

```
    omega_n(Mode_No) =
cant(Mode_No)^2*sqrt(E*Iy/(rho_Poly*W_beam*t_beam*L_beam^4)); % Natural
frequencies of vibration
end

%%%%%%%%%%%% Pressure Mode Shapes  %%%%%%%%%%%%%%%%%

i = sqrt(-1);
syms x y a4 a5 a6 a7 a8 a9 a10 a11 a12 a13 a14 a15 a16 SQ_No
aa = [a4 a5 a6 a7 a8 a9 a10 a11 a12 a13 a14 a15 a16];

Const2 = Pa*W_beam*L_beam^4/(E*Iy*h0);
alpha = 5.5; % Fitting parameter used for airflow damping


% Pressure distribution function in X and Y directions
% P(X) = (X-1)(a4*X^4 + a5*X^5 + ...)
% a4, a5, ... unknown coefficients to be determined (degrees of freedom)
% P(Y) = 1 - 4*B^2*Y^2
% B: aspect ratio

    Beta = L_beam/W_beam; % Beam aspect ratio
    N_C = 9; % Number of degrees of freedom for the P(X)


    for jj = 1:N_C
        XXX(jj,1) = x^(jj+3);
    end

    PX = (x-1)*(aa(1:N_C)*XXX);
    PY = 1 - 4*Beta^2*y^2;

    for l = 1:No_Mode
        PP(l) = eval(int(Normalized_W(l),x,0,1));
    end

    % Left hand side of the Reynolds' Equation
    LEFT = (6*epsilon*x)*diff(PX,x,1)*PY +
(1+3*epsilon*x^2)*(diff(PX,x,2)*PY + PX*diff(PY,y,2)) -
i*(1+epsilon*x^2)*SQ_No*PX*PY;
    % Left hand side of Reynolds' Equation calculated at y=0 (mid line)
    LEFT_0 = subs(LEFT,y,0);

    for jj = 1:N_C
        LEFT_0_X(jj) = subs(LEFT_0,x,jj/N_C);
    end

    for k = 1:N_C
        for jj = 1:N_C
            Coef_Mat(k,jj) = diff(LEFT_0_X(k),aa(jj),1);
        end
```

```
    end

    for k = 1:No_Mode
        for jj = 1:N_C
           RIGHT_X(jj) = subs(Normalized_W(k),x,jj/N_C);
        end
        COEF(k,:,:) = (inv(Coef_Mat)*(i*SQ_No*RIGHT_X.'));
    end


    for k = 1:No_Mode
        for jj = 1:No_Mode
            I(k,jj) = (2/3)*(int(Normalized_W(k)*(x-
1)*(COEF(jj,:,:)*XXX),x,0,1));
        end
    end

%%%%%%%%%%%%%%%%%%%%%%%%%%%%%%%%%%%%%%%%%%%%%%%%%%%%%%%%%%%%%%%%%%%%%%%%%%%%%%%
%%%%%%
Max_freq = 120000; %Max frequency of interest
Freq_step_size = 4000; % Step size
Vector_size = Max_freq/Freq_step_size; % Frequency vector size

for j = 1 : Vector_size

    omega = 2*pi*j*Freq_step_size;
    SQ = 12*mu*omega*L_beam^2/(Pa*h0^2); %Squeeze Number
    Const1 = rho_Poly*W_beam*t_beam*L_beam^4/(E*Iy); % Refer to Page 43 of
Sohrab's thesis
    Q_H = rho_Poly*t_beam*omega^2*Z0/(Pa); % Harmonic load due to
substrate vibration
    Ca = pi*alpha*(1.5*mu + (3/8)*W_beam*sqrt(2*rho_air*mu*omega)); %
Airflow damping Coefficient
    Const3 = i*omega*Ca*Z0/(Pa*W_beam);

    II = PP.*Q_H;
    III = PP.*Const3;

    %%%%%%%  AA = HH^-1*FF   AA: Mode shape amplitude
    %%%%%%%  Refer to page 44 of Sohrab's thesis
    HH = [ALPHA(1) - Const1*omega^2 - (Const2*subs(I(1,1),SQ)) +
i*omega*h0*Ca*Const2/(Pa*W_beam),            -(Const2*subs(I(1,2),SQ));
          -(Const2*subs(I(2,1),SQ)),               ALPHA(2) -
Const1*omega^2 - (Const2*subs(I(2,2),SQ)) +
i*omega*h0*Ca*Const2/(Pa*W_beam)];
    FF = Const2.*[(II(1)-III(1)) (II(2)-III(2))].';
    AA(j,:) = inv(HH)*FF;

    %%%%%%% Damping Factor and Spring Force Calculator
    zeta(j) = (omega_n(1)/omega)*imag(HH(1,1))/(2*ALPHA(1));
    zeta_a(j) = omega_n(1)*h0*Const2*Ca/(Pa*W_beam)/(2*ALPHA(1));
```

```
    zeta_sq(j) = -
(omega_n(1)/omega)*imag(Const2*subs(I(1,1),SQ))/(2*ALPHA(1));
    spring(j) = -real(Const2*subs(I(1,1),SQ))/(2*ALPHA(1));
end


%%%%%%%%%%%%%%%%%%%%%%%%%%%%%%%%%%%%%%%%%%%%%%%%%%%%%%%%%%%%%%%%%%%%%%%%%%%%%%%
%%%%%%%%%%%%%%%%%%          Plotting Results        %%%%%%%%%%%%%%%%%%%%%%%%%%
%%%%%%%%%%%%%%%%%%%%%%%%%%%%%%%%%%%%%%%%%%%%%%%%%%%%%%%%%%%%%%%%%%%%%%%%%%%%%%%

%%%%% Pressure Mode Shapes
for jj = 1:2
    figure(3+jj)
    P(jj) =(x-1)*(subs(COEF(jj,:,:),SQ)*XXX)*(1 - 4*Beta^2*y^2);
    ezmeshc((real(P(jj)))*Pa,[0,1,-1/(2*Beta),1/(2*Beta)],200)
    title('')
    colorbar
    figure(5+jj)
    ezmeshc((imag(P(jj)))*Pa,[0,1,-1/(2*Beta),1/(2*Beta)],200)
    title('')
    colorbar
end

%%%%% Frequency Response
    freq = [1:Vector_size]*Freq_step_size;
    A1 = (AA(:,1));
    A2 = (AA(:,2));
    figure(1)
    hold on

plot(freq,abs(subs(Normalized_W(1),x,spot_ratio)*A1+subs(Normalized_W(2),x
,spot_ratio)*A2)*h0/Z0,'g -')

rrr=abs(subs(Normalized_W(1),x,spot_ratio)*A1+subs(Normalized_W(2),x,spot_
ratio)*A2)*h0/Z0;
```

Optical Transfer Function Calculator

```
clc
clear
close all

%%%%%%%%% Input Data  %%%%%%%%%
lambda_nm = 632.8;  % Laser wavelength in nm
lambda = lambda_nm*1e-9;
f = 45000; % Vibration frequency
k = 2*pi/lambda; % Constant that comes from the phase of the Electric Field
h0 = 2e-6;  % Initial air gap
disp = [632.8e-9 120e-9 20e-9]; % Displacement amplitude
scale_factor=0.13691955813280;
device = 1; % 1 for PolyMUMPs, 2 for Nitride
thickness = 2e-6; % Structural Layer thickness


%%%%%%%%%%%% Power reflectance calculation %%%%%%%%%%%%%%%%
wt=linspace(0,2/f,1000);
for q = 1 : length(disp)

    for m = 1:length(wt)
        gap(m) =  h0 + disp(q)*sin(2*pi*f*wt(m));
    end
    gaps(q,:) = gap;
    [R,T,layer3] =
multilayer_film_calculator(lambda_nm,lambda,k,gap,device,thickness);
    Rs(q,:) = R;
    name_legend(q) = strcat({'disp = '},num2str(round(1e9*disp(q))),{' nm'});
end


%%%%%%%%%%%%%%%%%% Plot Results %%%%%%%%%%%%%%%%%%
color_plot = ['k' 'r' 'g' 'g' 'm'];
for q = 1:length(disp)
    subplot(2,1,2);
    plot(wt,scale_factor*Rs(q,:),color_plot(q)); % Plot the power reflectance
vs. time
    hold on;
end

for q = 1:length(disp)
    subplot(2,1,1);
    plot(1e9*gaps(q,:),scale_factor*Rs(q,:),color_plot(q)); % Plot the power
reflectance vs. gap height
    hold on;
end


subplot(2,1,2);
title('Interferometric Optical Signal');
```

```
xlabel('Time [ sec ]');
ylabel('Reflectance');
hold off; grid
legend('\delta_r = 120\mum','\delta_r = 20\mum');


subplot(2,1,1)
title('Transfer Function');
xlabel('Air gap [ nm ]');
ylabel('Reflectance');
grid
% Drawing a vertical line at X = initial airgap
XX = ones(1,10)*h0;
YY = linspace(0,scale_factor*(max(Rs(1,:))+.1),10);
line(XX*1e9,YY,'LineWidth',1)



%%%%%%%%%%%%%%%%%%%%%%%%%%%%%%%%%%%%%%%%%%%%%%%%%%%%%%%%%%%%%%%%%%%%%%%%%%%%%%%
%%%%%%%%%%%%%%%%%%%%%%%%%%%%%%%%%%%%%%%%%%%%%%%%%%%%%%%%%%%%%%%%%%%%%%%%%%%%%%%
% Function to determine the reflectance and transmission as a function of %
%                              the air gap                                 %
%%%%%%%%%%%%%%%%%%%%%%%%%%%%%%%%%%%%%%%%%%%%%%%%%%%%%%%%%%%%%%%%%%%%%%%%%%%%%%%

function [R,T,layer3] = calc_ref(lambda_nm,lambda,k,gap,device,thickness)

layers = 2; % Number of optical layers (3: for PolyMUMPs, 2: for nitride
device)
p = 0:layers+1;

if device ==1
    n = [1;4;1;2.19;3.8411+j*0.0167]; %refractive index  [Air, Polysilicon,
Air, Silicon nitride, Silicon (substrate)]
elseif device == 2
    n = [1;2.0737;1;3.8411+j*0.0167]; %refractive index  [Air, Silicon
nitride, Air, Silicon (substrate)]
end

% Mi = Reflection matrix for layer i
% layeri = Layer i thickness

layer2 = thickness;  % Thickness of the cantilever beam
M2 = [cos(k*layer2*n(2)) (-j/n(2))*sin(k*layer2*n(2));-
j*n(2)*sin(k*layer2*n(2)) cos(k*layer2*n(2))];

if device == 1
    layer4 = 0.6*1e-6; % The insulator layer thickness (this layer does not
exist in the nitride devices)
    M4 = [cos(k*layer4*n(4)) (-j/n(4))*sin(k*layer4*n(4));-
j*n(4)*sin(k*layer4*n(4)) cos(k*layer4*n(4))];
end
```

```
for i = 1 : length(gap);

    layer3(i)=gap(i);
    % Reflection matrix for the air gap layer
    M3 = [cos(k*layer3(i)*n(3)) (-j/n(3))*sin(k*layer3(i)*n(3));-
j*n(3)*sin(k*layer3(i)*n(3)) cos(k*layer3(i)*n(3))];

    % Calculating the total reflection matrix
    if device == 1
        M = M2*M3*M4;
    elseif device == 2
        M = M2*M3;
    end

   % Reflection coefficient
   ref(i) = ((M(1,1)+M(1,2)*n(end))*n(1) - M(2,1) -
M(2,2)*n(end))/((M(1,1)+M(1,2)*n(end))*n(1) + M(2,1) + M(2,2)*n(end));
   % Reflectance
   R(i) = (abs(ref(i)))^2;
   % Transmission coefficient
   tran(i) = 2*n(1)/( (M(1,1) + M(1,2)*n(end))*n(1) + M(2,1) + M(2,2)*n(end)
);
   % Transmitance
   T(i) = (real(n(end))/n(1))*(abs(tran(i)))^2;
   RT(i) = R(i)+T(i);
end

clear gap
```

Pressure Fitting

```
clc
close all
clear


load('Experimental.mat')
a(1,:)=Exp(:,1)';

freq=freq;
f =[0:5000:120000];


    [para] = fminsearch('error_func',1e5,[],freq,a(1,:));
    PP = num2str(para*14.69/1e5)
    pres(i) = para
    figure
    RR(:,i) = plotter2(para,f);
    plot(f,RR(:,i),'r')
    title('')
    hold on
    plot(freq,a(i,:),'.')
    axis([ 0 120000 0 3])
    xlabel('f [kHz]')
    ylabel('relative motion')
    title(['fitted Pressure: ',PP,' psi'])
    grid
    legend('Fitted data','Experimental data')

%%%%%%%%%%%%%%%%%%%%%%%%%%%%%%%%%%%%%%%%%%%%%%%%%%%%%%%%%%%%%%%%%%%%%%%%%%%%%%%
%                                 Error Function                                %
%%%%%%%%%%%%%%%%%%%%%%%%%%%%%%%%%%%%%%%%%%%%%%%%%%%%%%%%%%%%%%%%%%%%%%%%%%%%%%%

function [error] = error_func(param,freq,Exp_data)

%%%%%%%%%%%%%%%%%%%%%%%% Input Data %%%%%%%%%%%%%%%%%%%%%%%%

    %%%%%%%%%%%%%%%%%%% Young Modulus & Density %%%%%%%%%
    E = 158e9;
    rho_Poly = 2330;

    %%%%%%%%%%%%%%%%%%% Cantilever Beam Dimensions %%%%%%
    L_beam = 263e-6;
    W_beam = 10e-6;
    t_beam = 1.42e-6;
    h0 = 2.75e-6;  %% Air gap at the anchor
    epsilon = -0.14;  %% Beam curvature
    Iy = W_beam*t_beam^3/12;
```

```
    %%%%%%%%%%%%%%%%%%% Spot Location %%%%%%%%%%%%%%%%%%%
    spot = 5e-6;  %% From the tip
    spot_ratio = (L_beam-spot)/L_beam;

    %%%%%%%%%%%%%%%%%%% Air Properties %%%%%%%%%%%%%%%%%%%
    Pa = param;
    mu = 1.8e-5;
    rho_air=(Pa/1e5)*1.3;


%%%%%%%%%%%%%%%% Structural Mode Shape %%%%%%%%%%%%%%%%%%
cant = [1.8762 4.6904 7.8549];  % beta_n*l refer to "Theory of Vibration with
application" pp. 273
ALPHA = cant.^4;
No_Mode = 2;
for Mode_No = 1:No_Mode
    bb = cant(Mode_No);
    W2 = [1.0018 .9976];
    Def(Mode_No) = ((cosh(bb*spot_ratio) - cos(bb*spot_ratio)) - ((cosh(bb) +
cos(bb))/(sinh(bb) + sin(bb)))*(sinh(bb*spot_ratio) -
sin(bb*spot_ratio)))/sqrt(W2(Mode_No));
    omega_n(Mode_No) =
cant(Mode_No)^2*sqrt(E*Iy/(rho_Poly*W_beam*t_beam*L_beam^4)); % Natural
frequencies of vibration
end


%%%%%%%%%%%%% Airflow Damping Calculator
Const2 = Pa*W_beam*L_beam^4/(E*Iy*h0);
alpha = 5.5;
for k = 1:2
    Ca = pi*alpha*(1.5*mu + (3/8)*W_beam*sqrt(2*rho_air*mu*omega_n(k)));
    Z(k) = omega_n(k)*h0*Const2*Ca/(Pa*W_beam)/(2*ALPHA(k));
end
%%%%% Airflow damping + Squeeze film damping
zeta = Z + [.33 .0361];

j=sqrt(-1);
OMEGA = 2*pi*freq;
int_phi = [.783 .4364];
for i = 1:length(OMEGA)

    A1 = ((OMEGA(i)/omega_n(1))^2*.783)/(1+2*j*zeta(1)*(OMEGA(i)/omega_n(1))-
(OMEGA(i)/omega_n(1))^2);
    A2 =
((OMEGA(i)/omega_n(2))^2*.4364)/(1+2*j*zeta(2)*(OMEGA(i)/omega_n(2))-
(OMEGA(i)/omega_n(2))^2);
    resp(i)= abs(Def(1)*A1+Def(2)*A2);
    err(i) = Exp_data(i) - resp(i);
end

error = dot(err,err);
```

```
%%%%%%%%%%%%%%%%%%%%%%%%%%%%%%%%%%%%%%%%%%%%%%%%%%%%%%%%%%%%%%%%%%%%%%%%%%%%%%%
%                                    Plotter                                    %
%%%%%%%%%%%%%%%%%%%%%%%%%%%%%%%%%%%%%%%%%%%%%%%%%%%%%%%%%%%%%%%%%%%%%%%%%%%%%%%
function [resp] = myerrorfun2(param,freq)

%%%%%%%%%%%%%%%%%%%%%%%% Input Data %%%%%%%%%%%%%%%%%%%%%%%%

    %%%%%%%%%%%%%%%%%%%% Young Modulus & Density %%%%%%%%%
    E = 158e9;
    rho_Poly = 2330;

    %%%%%%%%%%%%%%%%%%%% Cantilever Beam Dimensions %%%%%%
    L_beam = 263e-6;
    W_beam = 10e-6;
    t_beam = 1.42e-6;
    h0 = 2.75e-6;  %% Air gap at the anchor
    epsilon = -0.14;  %% Beam curvature
    Iy = W_beam*t_beam^3/12;

    %%%%%%%%%%%%%%%%%%%% Spot Location %%%%%%%%%%%%%%%%%%%%
    spot = 5e-6;  %% From the tip
    spot_ratio = (L_beam-spot)/L_beam;

    %%%%%%%%%%%%%%%%%%%% Air Properties %%%%%%%%%%%%%%%%%%%%
    Pa = param;
    mu = 1.8e-5;
    rho_air=(Pa/1e5)*1.3;


%%%%%%%%%%%%%%%% Structural Mode Shape %%%%%%%%%%%%%%%%%%%
cant = [1.8762 4.6904 7.8549];  % beta_n*l refer to "Theory of Vibration with
application" pp. 273
ALPHA = cant.^4;
No_Mode = 2;
for Mode_No = 1:No_Mode
    bb = cant(Mode_No);
    W2 = [1.0018 .9976];
    Def(Mode_No) = ((cosh(bb*spot_ratio) - cos(bb*spot_ratio)) - ((cosh(bb) +
cos(bb))/(sinh(bb) + sin(bb)))*(sinh(bb*spot_ratio) -
sin(bb*spot_ratio)))/sqrt(W2(Mode_No));
    omega_n(Mode_No) =
cant(Mode_No)^2*sqrt(E*Iy/(rho_Poly*W_beam*t_beam*L_beam^4)); % Natural
frequencies of vibration
end


%%%%%%%%%%%%% Airflow Damping Calculator
Const2 = Pa*W_beam*L_beam^4/(E*Iy*h0);
alpha = 5.5;
for k = 1:2
    Ca = pi*alpha*(1.5*mu + (3/8)*W_beam*sqrt(2*rho_air*mu*omega_n(k)));
    Z(k) = omega_n(k)*h0*Const2*Ca/(Pa*W_beam)/(2*ALPHA(k));
```

```
end
%%%%% Airflow damping + Squeeze film damping
zeta = Z + [.33 .0361];

j=sqrt(-1);
OMEGA = 2*pi*freq;
int_phi = [.783 .4364];
for i = 1:length(OMEGA)

    A1 = ((OMEGA(i)/omega_n(1))^2*.783)/(1+2*j*zeta(1)*(OMEGA(i)/omega_n(1))-
(OMEGA(i)/omega_n(1))^2);
    A2 =
((OMEGA(i)/omega_n(2))^2*.4364)/(1+2*j*zeta(2)*(OMEGA(i)/omega_n(2))-
(OMEGA(i)/omega_n(2))^2);
    resp(i)= abs(Def(1)*A1+Def(2)*A2);

end
```

Bibliography

1. Pulliam W., Russler P., Fielder R., "High-Temperature, High Bandwidth, Fiber-Optic, MEMS Pressure Sensor Technology for Turbine Engine Component Testing", Fiber Optic Sensor Technology and Applications 2001

2. Breuer K., "MEMS Sensors for Aerodynamic Applications – the Good, the Bad (and the Ugly)", AIAA 2000-0251

3. Nieva P. "Design and Analysis of MEMS Based Micro-Opto-Mechanical Vibration Sensors", PhD Dissertation, Electrical Eng. Dept., Northeastern University, August 2004

4. Eaton W. P., Smith J. H., "Micromachined pressure sensors: review and recent development", Smart Mater. Struct. 6 (1997) 530 – 539

5. Frobenius W. D., Sanderson A. C., Nathanson H. C., "A microminiature, solid-state capacitive blood pressure sensor transducer with improved sensitivity" IEEE Biomed. Eng. BME-20 312 – 316

6. Xu J., Pickrell G., Wang X., Peng W., "A Novel Temperature-Insensitive Optical Fiber Pressure Sensor for Harsh Environments", IEEE Photonics Tech. Letters, 4 (2005) 870 – 872

7. Chan M. A., Collins S. D., "A micromachined pressure sensor with fiber-optic interferometric readout", Sensors and Actucators A, 43 (1994) 196 – 201

8. Elwnspoek M., Wiegerink R., "Mechanical Microsensors", Springer 2001

9. Jiang L., Wong M., Zohar Y., "Micromachined Polycrystalline Thin Film Temperature Sensors", Meas. Sci. Technol. 10 (1999) 653 – 664

10. Fraden J., "Handbook of Modern Sensors", AIP Press 1997

11. Bernstein J., Miller R., Kelley W., and Ward P., "Low-Noise MEMS Vibration Sensor for Geophysical Applications" J. MEMS, Vol. 8, No. 4, Dec1999

12. Thomson W. T., "Theory of Vibration with Application" Prentice Hall 1998

13. Waters R., Aklufi M., "Micromachined Fabry-Perot interferometer for motion detection", Applied Physicss Letters 81 (2002) 3320 – 3322

14. Hall A., Okandan M., Degertekin F., "Surface and Bulk-Silicon-Micromachined Optical Displacement Sensor Fabricated With the SwIFT-Lite Process" J. MEMS 15 (2006) 770 – 776

15. Hamrock B. J. "Fundamentals of Fluid Film Lubrication", McGraW-Hill 1994

16. C. Zhang, G. Xu and Q. Jiang, "Characterization of the Squeeze Film Damping Effect on the Quality Factor of a Microbeam Resonator", J. Micromech. Microeng. 14 (2004) 1302-1306

17. H. Nayfeh, M. I. Younis, "A new approach to the modeling and simulation of flexible structures under the effect of squeeze-film damping", J. Micromech. Microeng. 14 (2004) 170-181

18. Pandey A. K., Pratap R., Chau S. F. "Analytical Solution of the modified Reynolds Equation for Squeeze Film Damping in Perforated MEMS Structures", Sensors and Actuators A 135 (2007) 839-848

19. M. Bao, H. Yang, Y. Sun1 and P. J. French, "Modified Reynolds' equation and analytical analysis of squeeze-film air damping of perforated structures", J. Micromech. Microeng. 13 (2003) 795–800

20. S. S. Mohite, H. Kesari, "Analytical Solution for the Stiffness and Damping Coefficients of Squeeze Films in MEMS Devices with Perforated Back Plates", J. Micromech. Microeng. 15 (2005) 2083-2092

21. H. Hosaka, K. Itao and S. Kuroda, "Evaluation of Energy Dissipation Mechanisms in Vibrational Microactuators",

22. H. Hosaka, K. Itao and S. Kuroda, “Damping characteristics of beam-shaped micro- oscillators”, Sensors and Actuators A 49 (1995) 87-95

23. H. Hosaka, Y. Katagiri, T. Hirota and K. Itao, “Micro-Optomechatronics”, (New York: Marcel Dekker 2005)

24. Mehner J.E.; Doetzel W.; Schauwecker B.; Ostergaard D., “Reduced Order Modelling of Fluid Structural Interactions in MEMS Based on Modal Projection Techniques” TRANSDUCERS '03. 12th International Conference on Solid-State Sensors, Actuators and Microsystems.

25. “PolyMUMPs Design Handbook”, MEMScAP, Version 11.0

26. Fowles G. R. “Introduction to Modern Optics”, Dover Publications, INC., New York 1989

27. “PolyMUMPs FAQ.”, MEMScAP, Revision 2